

# Cells in the Polyaneuploid Cancer Cell State are Pro-Metastatic

Mikaela M. Mallin<sup>1,2\*</sup>, Louis T.A. Rolle<sup>1</sup>, Michael J. Schmidt<sup>3</sup>, Shilpa Priyadarsini Nair<sup>1</sup>, Amado J. Zurita<sup>4</sup>, Peter Kuhn<sup>3,5,6,7,8,9</sup>, James Hicks<sup>3,5,9</sup>, Kenneth J. Pienta<sup>1,2</sup>, Sarah R. Amend<sup>1,2</sup>

<sup>1</sup>Cancer Ecology Center, James Buchanan Brady Urological Institute, Johns Hopkins Medical Institute, Baltimore, MD, USA

<sup>2</sup>Cellular and Molecular Medicine Graduate Training Program, Johns Hopkins School of Medicine, Baltimore, MD, USA

<sup>3</sup>Convergent Science Institute in Cancer, Michelson Center for Convergent Bioscience, Dornsife College of Letters, Arts and Sciences, University of Southern California, Los Angeles, CA, USA

<sup>4</sup>Department of Genitourinary Medical Oncology, The University of Texas MD Anderson Cancer Center, Houston, Texas

<sup>5</sup>Department of Biological Sciences, Dornsife College of Letters, Arts, and Sciences, University of Southern California, Los Angeles, CA, USA

<sup>6</sup>Department of Biomedical Engineering, Viterbi School of Engineering, University of Southern California, Los Angeles, CA, USA

<sup>7</sup>Department of Aerospace and Mechanical Engineering, Viterbi School of Engineering, University of Southern California, Los Angeles, CA, USA

<sup>8</sup>Institute of Urology, Catherine & Joseph Aresty Department of Urology, Keck School of Medicine, University of Southern California, Los Angeles, CA, USA

<sup>9</sup>Norris Comprehensive Cancer Center, Keck School of Medicine, University of Southern California, Los Angeles, CA 90033, USA

## \*Correspondence:

Mikaela M. Mallin  
Mmallin1@jhmi.edu

## Authors' Contributions:

M.M.M: Conceptualization, Formal Analysis, Investigation, Methodology, Validation, Visualization, Writing – Original Draft; L.T.A.R: Investigation, Writing – Review and Editing; M.J.S: Formal Analysis, Investigation, Visualization, Writing – Review and Editing; S.P.N: Investigation, A.J.Z: Writing-Review and Editing; P.K: Funding Acquisition, Writing – Review and Editing; J.H: Supervision, Funding

47 Acquisition; K.J.P: Conceptualization, Funding Acquisition, Writing – Review and  
48 Editing; S.R.A: Funding Acquisition, Writing – Review and Editing.

49

#### 50 **Competing Interests:**

51 M.M.M. has no disclosures. L.T.A.R. has no disclosures. M.J.S has no  
52 disclosures. S.P.N. has no disclosures. ruA. J. Z. has no disclosures. P.K. discloses  
53 ownership in Epic Sciences. J.H discloses he is a member of the Clinical Advisory  
54 Board of Epic Sciences. K.J.P. discloses that he is a consultant to Cue Biopharma, Inc.,  
55 an equity holder in PEEL therapeutics, and a founder and equity holder in Keystone  
56 Biopharma, Inc. and Kreffect, Inc. S.R.A. discloses that she is an equity holder in  
57 Keystone Biopharma, Inc.

58

#### 59 **Ethics Statement:**

60 All animal experiments were reviewed and approved by the Johns Hopkins  
61 Animal Care and Use Committee. Human elements of this study were approved by the  
62 corresponding institutional review boards and were conducted in accordance with  
63 ethical principles founded in the Declaration of Helsinki. All patients gave written  
64 informed consent.

65

#### 66 **Funding:**

67 P.K and J.H were supported by the National Cancer Institute’s Norris  
68 Comprehensive Cancer Center (CORE) Support 5P30CA014089-40. K.J.P was  
69 supported by National Cancer Institute grants U54CA143803, CA163124, CA093900,  
70 and CA143055, and the Prostate Cancer Foundation. S.R.A. was supported by the US  
71 Department of Defense CDMRP/PCRP (W81XWH-20-10353 and W81XWH-22-1-  
72 0680), the Patrick C. Walsh Prostate Cancer Research Fund, and the Prostate Cancer  
73 Foundation.

74

#### 75 **Acknowledgements:**

76 The authors would like to acknowledge Ana Aparicio and Paul Corn for their  
77 critical contributions. The authors would also like to thank the patients and their  
78 caregivers who consented to this study, as well as the clinical research staff who  
79 contributed. The authors also thank the members of the Cancer Ecology Center for  
80 thoughtful conversation and invaluable feedback.

81

#### 82 **Data Availability Statement:**

83 Nearly all data generated in this study are available within the article and its  
84 supplementary data files. Detailed data regarding the 247-panel cytokine array are  
85 available upon request from the corresponding author.

86

#### 87 **Abstract:**

88 There remains a large need for a greater understanding of the metastatic  
89 process within the prostate cancer field. Our research aims to understand the adaptive  
90 – ergo potentially metastatic – responses of cancer to changing microenvironments.  
91 Emerging evidence has implicated a role of the Polyaneuploid Cancer Cell (PACC)  
92 state in metastasis, positing the PACC state as capable of conferring metastatic

93 competency. Mounting *in vitro* evidence supports increased metastatic potential of cells  
94 in the PACC state. Additionally, our recent retrospective study of prostate cancer  
95 patients revealed that PACC presence in the prostate at the time of radical  
96 prostatectomy was predictive of future metastatic progression. To test for a causative  
97 relationship between PACC state biology and metastasis, we leveraged a novel method  
98 designed for flow-cytometric detection of circulating tumor cells (CTCs) and  
99 disseminated tumor cells (DTCs) in subcutaneous, caudal artery, and intracardiac  
100 mouse models of metastasis. This approach provides both quantitative and qualitative  
101 information about the number and PACC-status of recovered CTCs and DTCs. Collating  
102 data from all models, we found that 74% of recovered CTCs and DTCs were in the  
103 PACC state. *In vivo* colonization assays proved PACC populations can regain  
104 proliferative capacity at metastatic sites following dormancy. Additional direct and  
105 indirect mechanistic *in vitro* analyses revealed a PACC-specific partial Epithelial-to-  
106 Mesenchymal-Transition phenotype and a pro-metastatic secretory profile, together  
107 providing preliminary evidence that PACCs are mechanistically linked to metastasis.  
108

#### 109 **Statement of Significance:**

110 We provide the first evidence that cells in the polyan euploid cancer cell state  
111 contribute to increased metastatic competency *in vivo*.  
112

#### 113 **Keywords:**

114 Polyaneuploid Cancer Cell (PACC), Polyploid Giant Cancer Cell (PGCC),  
115 Metastasis, Metastatic Competency, Circulating Tumor Cell (CTC), Disseminated  
116 Tumor Cell (DTC), partial-Epithelial-to-Mesenchymal-Transition (pEMT), *in vivo*  
117 Metastatic Models  
118

#### 119 **I. Introduction:**

120  
121 Though early detection of prostate cancer favors diagnosis of eradicable  
122 localized disease, metastatic prostate cancer remains lethal and incurable. Metastatic  
123 disease arises when metastatically-competent cells in the primary tumor i) invade local  
124 tissue, ii) intravasate into the vasculature, iii) survive circulatory transit, iv) extravasate  
125 into a distant organ, and v) colonize that organ (1). In 2024, it is projected that over  
126 35,000 men in the US will die from metastatic prostate cancer (2). Clearly, there  
127 remains a large need for a greater understanding of the metastatic process within the  
128 prostate cancer field. One approach relies on understanding how tumor  
129 microenvironmental stressors constantly influence the adaptive potential of cancer cells,  
130 potentially driving phenotypes with increased metastatic potential.

131 Emerging evidence has highlighted the role of the Polyaneuploid Cancer Cell (or  
132 PACC) state as a phenotype of metastatically competent cells (3-7). Cells in the PACC  
133 state (also termed Polyploid Giant Cancer Cells, Multinucleate Giant Cells, and  
134 Pleomorphic Cells) exhibit a transient and adaptive cellular response to genotoxic  
135 stress. Most notably, the PACC state is characterized by an increase in genomic  
136 content coincident with an indefinite pause in cell division (8). Canonically, it is  
137 understood that genotoxic stress results in a G2/M cell cycle checkpoint stall that allows  
138 for an attempt at genomic repair, and in the event of failure, promotes apoptosis. Cells

139 in the PACC-state adopt an interphase-restricted cell cycle following an expected  
140 stress-induced G2/M pause (9-11). This alternative cell cycle pattern, termed an  
141 endocycle, consists of subsequent cycles of G1, S, and G2 phases without any  
142 intervening M phases (12). In addition to explaining the increase in genomic content and  
143 lack of cell division, an endocycle also explains the vast nuclear and cytoplasmic  
144 enlargement typical of cells in the PACC state, which together create a distinct  
145 morphological phenotype useful in identifying PACCs in cell culture as well as  
146 histopathologic contexts. Indeed, these morphological features have been frequently  
147 used as markers of the PACC state phenotype, which has been observed to arise in  
148 various cell lines (prostate, breast, ovarian, brain, and melanoma, among others) in  
149 response to multiple classes of anti-cancer stressors (13-18).

150 We and others have published data supporting that cells in the PACC state have  
151 increased metastatic potential. Functionally, Xuan et. al. has reported that breast cancer  
152 MDA-MB-231 PACCs exhibit a persistent migratory phenotype driven by an enriched  
153 Vimentin filament network (19, 20). More recently, we have shown that prostate cancer  
154 PC3 PACCs demonstrate an identical motility phenotype to that observed by Xuan et al.  
155 that can be influenced by presence of a chemotactic gradient (21). In mice, Zhang et. al.  
156 showed that serial metastatic passage of PC3 cells increased not only the cells'  
157 metastatic rates but also their percentage PACC makeup with each cycle of selection  
158 (22).

159 Clinical research has also indicated a potential role for PACCs in contributing to  
160 metastasis. Stromal-invasive PACCs identified by histology were more frequently  
161 identified in patients with metastatic (vs. nonmetastatic) ovarian cancer: PACCs were  
162 found in 18/21 high-grade primary tumors from patients with metastases, but only 6/26  
163 low-grade primary tumors from patients without metastasis (23). Similar trends have  
164 been reported in prostate cancer; of 27 patients with PACC-positive cases of prostate  
165 cancer, all 27 had Gleason-scores of 9 or 10, indicating that presence of cells in the  
166 PACC state is linked to more aggressive disease (24). An independent study published  
167 nearly identical findings: of 30 patients presenting with PACC-positive cases of prostate  
168 cancer, all 30 had Gleason-scores of 9 or 10, and 11 patients were dead at a median of  
169 8 months after diagnosis (25). The Michigan Legacy Tissue program identified PACCs  
170 in all 16 osseous and non-osseous metastatic sites of 5 randomly selected cases of  
171 prostate cancer, and most PACCs identified were concentrated around tumor hotspots  
172 (26). Most recently, we reported that presence of PACCs in the primary tumor at the  
173 time of radical prostatectomy was predictive of future metastatic progression in men  
174 with prostate cancer (27). These studies reveal a correlation between PACC state  
175 biology and metastasis.

176 To test for a causative relationship between PACC state biology and metastasis,  
177 we leveraged our recently published flow cytometry method designed for the detection  
178 of rare circulating tumor cells (CTCs) and disseminated tumor cells (DTCs) in metastatic  
179 mouse models (28). This approach is powerful because it provides both quantitative and  
180 qualitative information about the number and PACC-status of metastasizing  
181 CTCs/DTCs recovered from animal tissues. We used various *in vivo* models to test  
182 distinct steps of the metastatic cascade. Measurement of spontaneous metastasis of  
183 blood CTCs and distant organ DTCs from subcutaneous tumors tested invasion,  
184 intravasation, and circulation survival (for CTCs), as well as extravasation (for DTCs).

185 Measurement of DTCs from caudal artery and tail vein injections specifically tested  
186 extravasation. Evaluation of primary tumor growth in subcutaneous models tested  
187 dormancy and colonization. Lastly, measurement of metastatic lesion outgrowth  
188 following intracardiac injection tested circulation survival, extravasation, dormancy, and  
189 colonization.

190 Across the various models, 75% of recovered CTCs and 72% of recovered DTCs  
191 were in the PACC state, as defined by a DNA content greater than 4N (>4N). Two *in*  
192 *vivo* colonization assays proved that PACC populations can regain proliferative capacity  
193 following long periods of dormancy, a phenomenon frequently observed and yet  
194 inadequately understood in the clinic. *In vitro* studies revealed a PACC-specific partial-  
195 Epithelial-to-Mesenchymal-Transition (pEMT) as a likely mechanism of increased  
196 metastatic behavior in PACCs. Notably, PACCs identified in the blood of human  
197 prostate cancer patients also demonstrated a pEMT phenotype characterized by co-  
198 expression of EpCAM and Vimentin. Additionally, an analysis of PACC-conditioned  
199 media and its effects on nonPACC cells indicated that a PACC-specific pro-metastatic  
200 secretory phenotype may increase metastatic potential of nonPACCs. Together, our  
201 results provide strong evidence that the clinically observed links between PACC  
202 presence and risk of metastasis move beyond mere correlation. Our data point to a  
203 combination of direct and indirect mechanisms that together support a causative  
204 relationship between PACCs and increased metastatic risk.

205

## 206 **II. Results:**

207

### 208 **The majority of circulating tumor cells are in the PACC state**

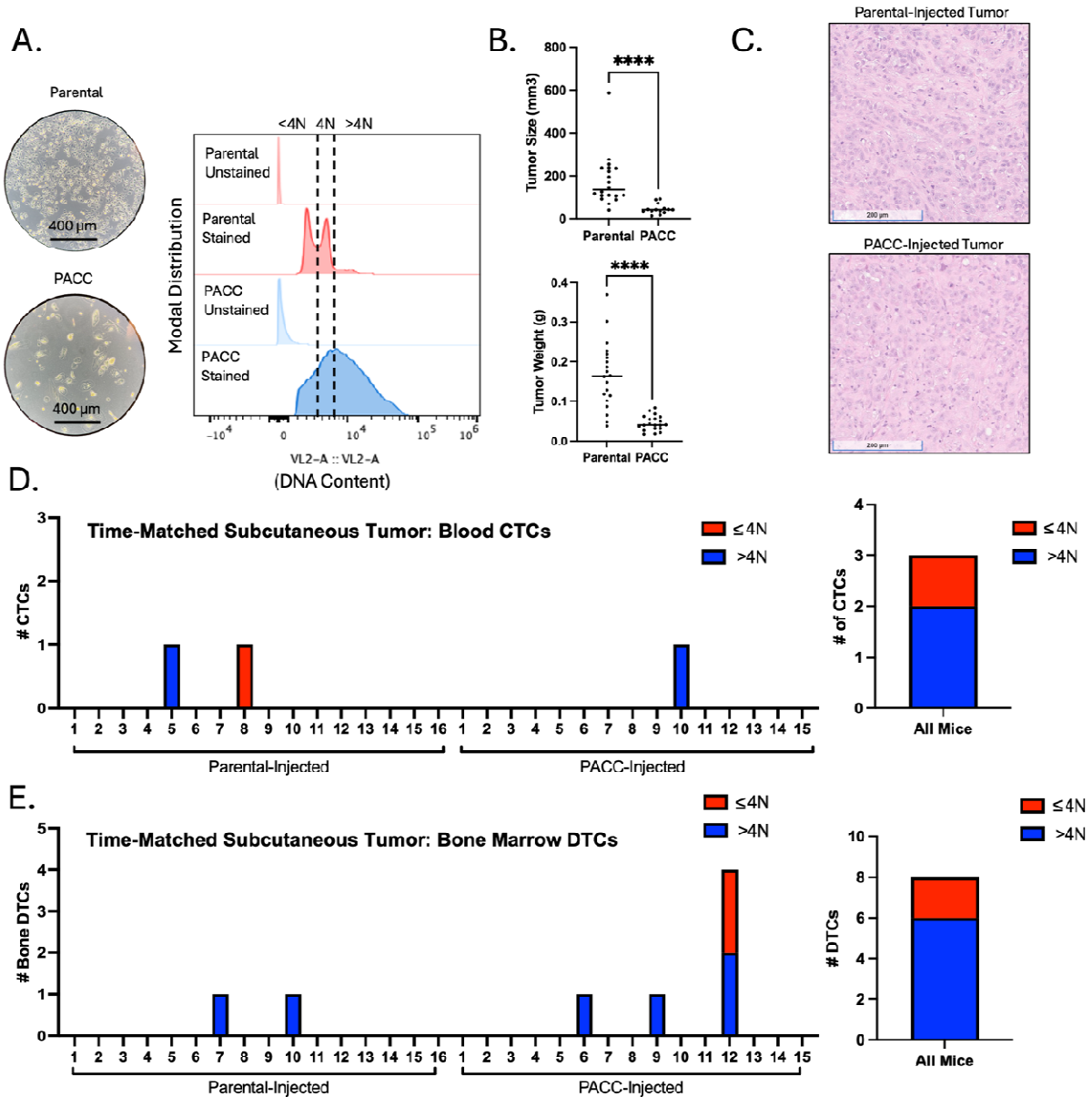
209

210 We used size-matched and time-matched subcutaneous murine metastasis  
211 models to measure the differential metastatic potential of PACCs through evaluation of  
212 CTCs recovered from the blood. Mice were injected subcutaneously with either parental  
213 cells or PACC-enriched cells confirmed to have increased ploidy at the population level  
214 (Figure 1A, 2A).

215 In a time-matched model, blood from each mouse was collected and analyzed 6  
216 weeks following tumor cell injection. At experimental endpoint, parental-injected mice  
217 produced larger tumors than PACC-injected mice (Figure 1B) probably (?) due to the  
218 transiently nonproliferative phenotype of PACCs abundant in the PACC-enriched  
219 population. At experimental endpoint, the proportion of PACCs to nonPACCs in each  
220 tumor equilibrated to similar levels (Figure 1C, appreciable by comparison of cell size).  
221 In total, 3 CTCs were recovered, 2 of which were in the PACC state (66%) (Figure 1D,  
222 Supplemental Figure S1).

223 To increase the number of recoverable CTCs, we repeated the experiment using  
224 a tumor size-matched model, in which the experimental endpoint of each mouse was  
225 independently determined. Blood was collected and analyzed when tumors reached  
226 approximately 350 mm<sup>3</sup> (Figure 2B). Again, at experimental endpoint, the proportion of  
227 PACCs to nonPACCs in each tumor equilibrated to similar levels (Figure 2C,  
228 appreciable by comparison of cell size). In total, 33 CTCs were recovered, 25 of which  
229 were in the PACC state (75%) (Figure D, Supplemental Figure S3). Altogether, these

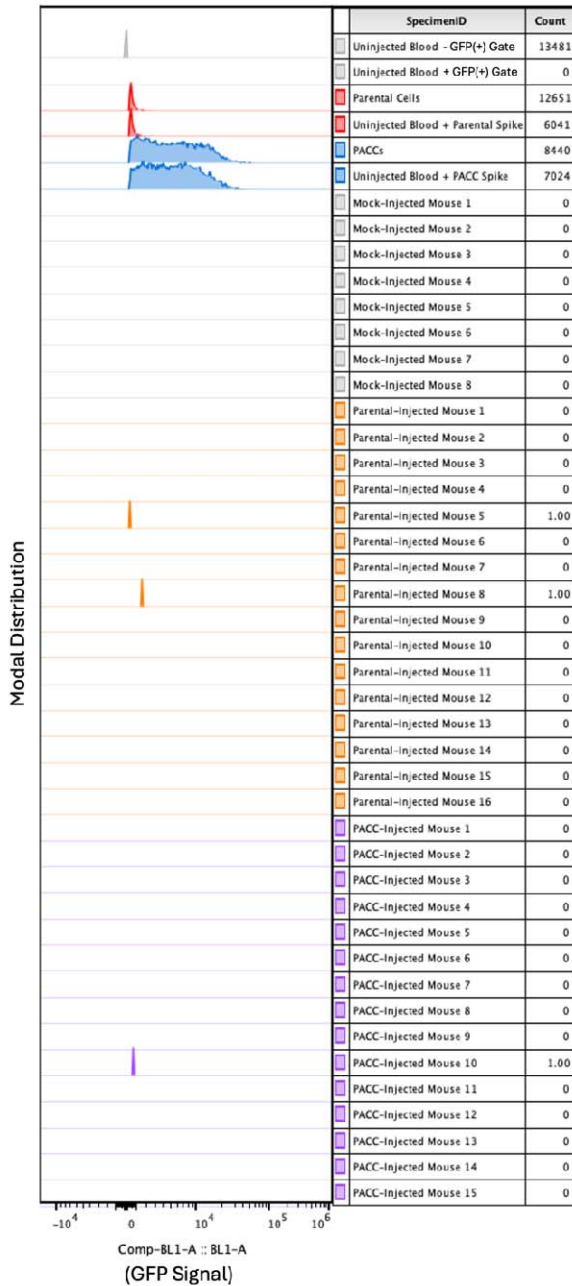
230 data confirm that i) PACCs can survive as CTCs in the context of spontaneous  
 231 metastasis, and ii) the majority of CTCs recovered in this context are in the PACC state.



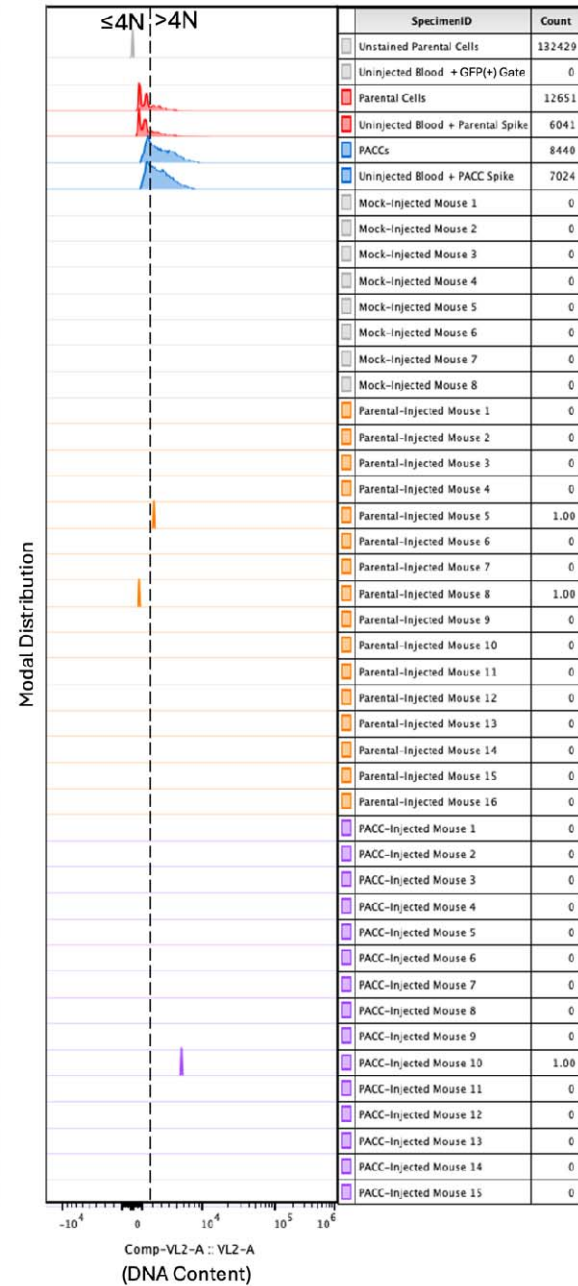
232  
 233 **Figure 1:**  
 234 Time-matched, subcutaneous injection of PC3-GFP-Luc parental population vs.  
 235 PACC-enriched population: A) Light microscopy photos and flow-cytometric ploidy  
 236 analysis of injected cells per injection group. B) Tumor volume and tumor weight  
 237 measurements per injection group at experimental endpoint. C) Representative H&E  
 238 photos of primary tumors per injection group. D) Enumeration of CTCs sourced from the  
 239 blood of each animal and quantification of % >4N CTCs vs. ≤4N CTCs. E) Enumeration

240 of DTCs sourced from the bone marrow of each animal and quantification of % >4N  
 241 DTCs vs.  $\leq 4N$  DTCs.

**A. Time-Matched Subcutaneous Tumor: Blood CTCs**



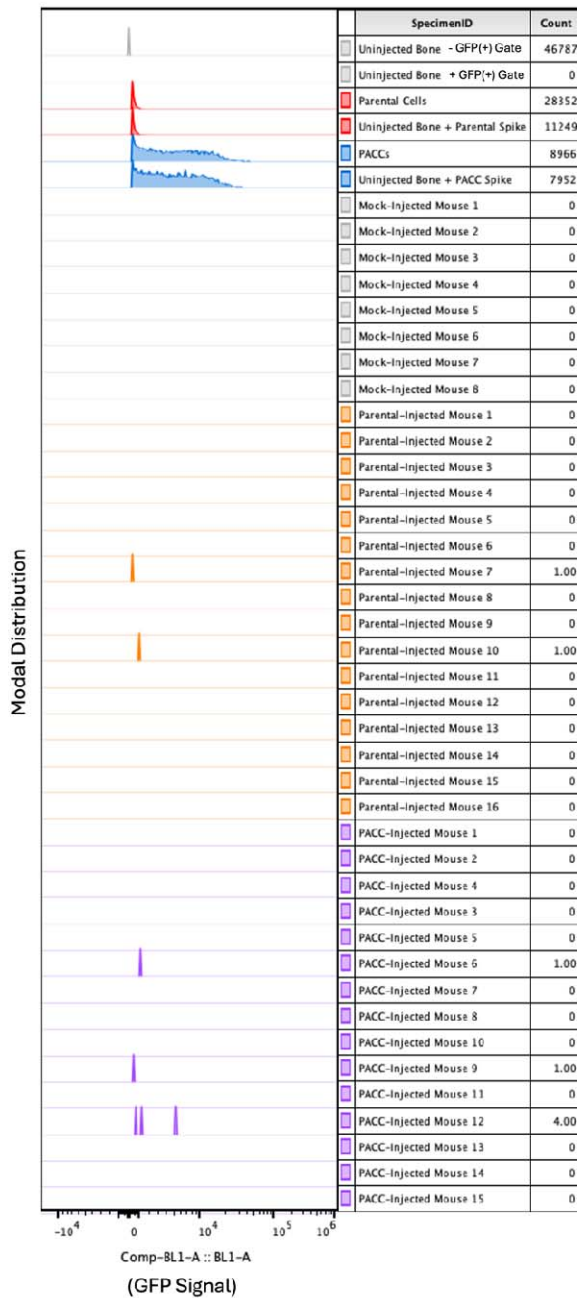
**B. Time-Matched Subcutaneous Tumor: Blood CTCs**



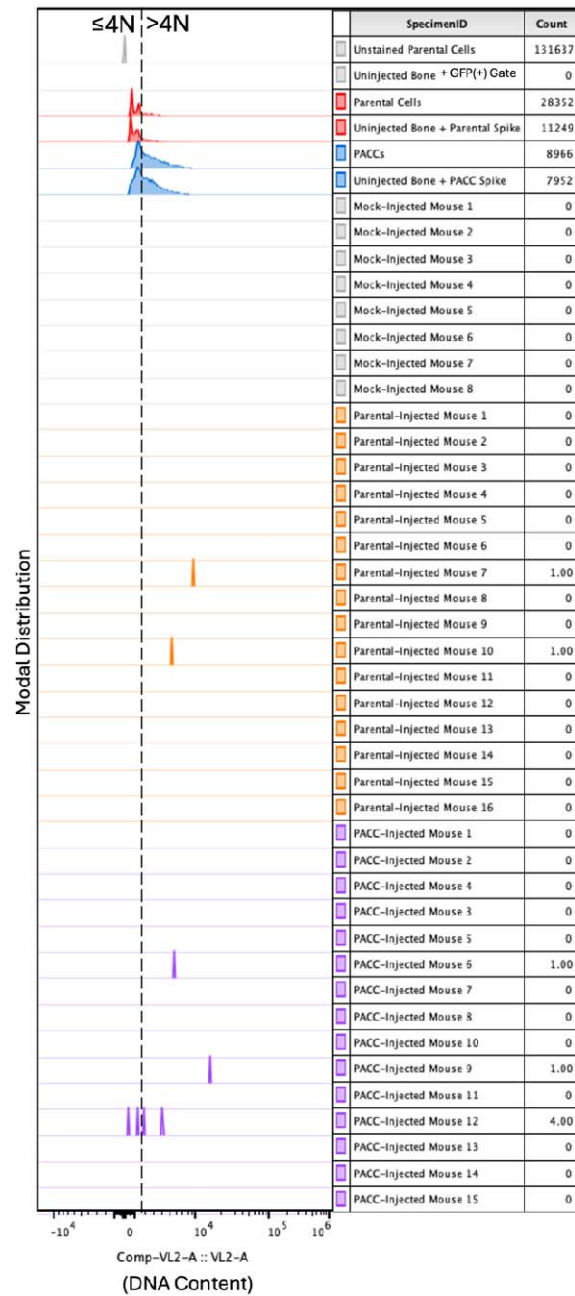
242 **Supplemental Figure S1:**

243 Time-matched, subcutaneous injection of PC3-GFP-Luc parental population vs.  
 244 PACC-enriched population: A) Raw cytometric data reporting GFP+ signal across all  
 245 blood samples. B) Raw cytometric data reporting DNA content of GFP+ cells across all  
 246 blood samples.

**A. Time-Matched Subcutaneous Tumor: Bone DTCs**



**B. Time-Matched Subcutaneous Tumor: Bone DTCs**



247 **Supplemental Figure S2:**

248 Time-matched, subcutaneous injection of PC3-GFP-Luc parental population vs.  
 249 PACC-enriched population: A) Raw cytometric data reporting GFP+ signal across all  
 250 bone marrow samples. B) Raw cytometric data reporting DNA content of GFP+ cells  
 251 across all bone marrow samples.

252  
 253



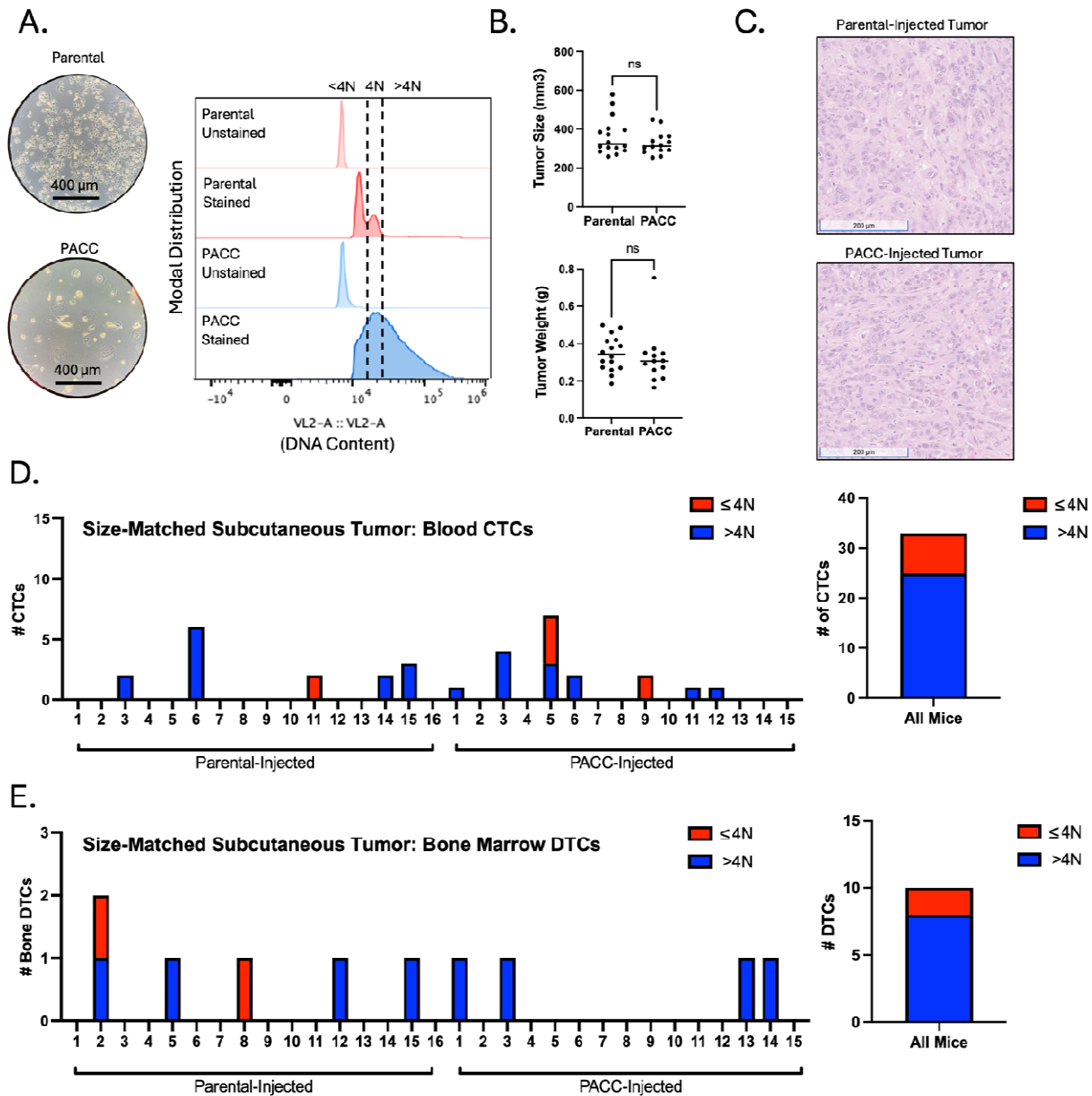
254

255 **The majority of disseminated tumor cells are in the PACC state**

256

257 The same two subcutaneous models used to measure blood CTCs were also  
258 used to quantify and characterize DTCs recovered from hind-limb bone marrow. Across  
259 both models, a majority of the DTCs recovered contained >4N DNA content, indicating  
260 they are in the PACC state. In the time-matched model, 8 bone marrow DTCs were  
261 recovered, 6 of which were in the PACC state (75%) (Figure 1E, Supplemental Figure  
262 S2). In the size-matched model, 10 DTCs were recovered, 8 of which were in the PACC  
263 state (80%) (Figure 2E, Supplemental Figure S4).

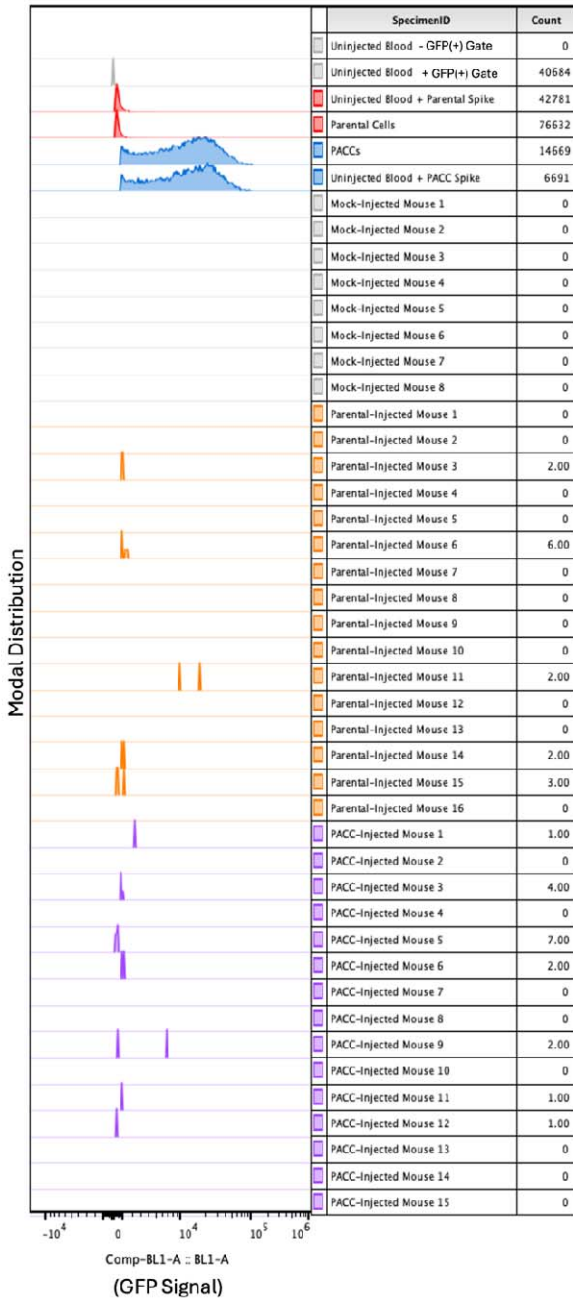
264 Subcutaneous tumor models are useful for investigating multiple steps of the  
265 metastatic cascade (i.e. invasion, intravasation, survival in the circulation, and  
266 extravasation) within one animal. However, they limit the ability to specifically query  
267 differential extravasation capacity between cell phenotypes owing to potential upstream  
268 bottlenecks that may differentially skew the numbers of each cell type surviving in the  
269 circulation. To directly measure the differential extravasation potential of PACCs, we  
270 used a caudal-artery injection model. Mice were injected with either parental cells or  
271 PACC-enriched cells confirmed to have increased ploidy at the population level (Figure  
272 3A). Bone marrow and lung tissue were collected and analyzed 3 days after injection.  
273 Caudal artery injection introduces cells directly into the vasculature and directs them to  
274 the hind limb bone marrow capillaries and lung capillaries, wherein they become lodged  
275 due to size. After 72 hours, lodged cells have either been cleared from the vasculature  
276 or, more rarely, have extravasated into surrounding tissue (Figure 3B). After 72 hours,  
277 81 DTCs were recovered from the bone marrow, 59 of which were in the PACC state  
278 (73%) (Figure 3C, Supplemental Figure S5). 132 DTCs were recovered from the lung,  
279 111 of which were in the PACC state (84%) (Figure 3D, Supplemental Figure S6). This  
280 data suggests that cells in the PACC state have increased extravasation potential  
281 compared to their nonPACC counterparts. As such, not only are PACCs uniquely adept  
282 at reaching and surviving within the circulatory system as CTCs, but they are also adept  
283 at extravasating into secondary site tissues.



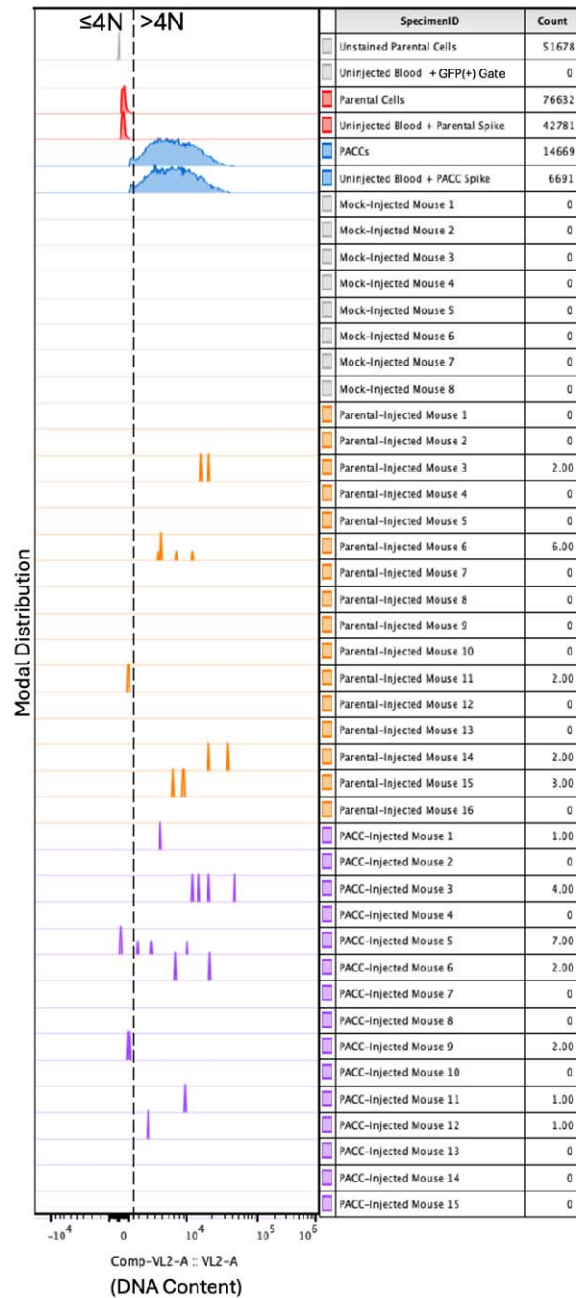
284 **Figure 2:**

285 Size-matched, subcutaneous injection of PC3-GFP-Luc parental population vs.  
 286 PACC-enriched population: A) Light microscopy photos and flow-cytometric ploidy  
 287 analysis of injected cells per injection group. B) Tumor volume and tumor weight  
 288 measurements per injection group at experimental endpoint. C) Representative H&E  
 289 photos of primary tumors per injection group. D) Enumeration of CTCs sourced from the  
 290 blood of each animal and quantification of %  $>4N$  CTCs vs.  $\leq 4N$  CTCs. E) Enumeration  
 291 of DTCs sourced from the bone marrow of each animal and quantification of %  $>4N$   
 292 DTCs vs.  $\leq 4N$  DTCs.

**A. Size-Matched Subcutaneous Tumor: Blood CTCs**



**B. Size-Matched Subcutaneous Tumor: Blood CTCs**

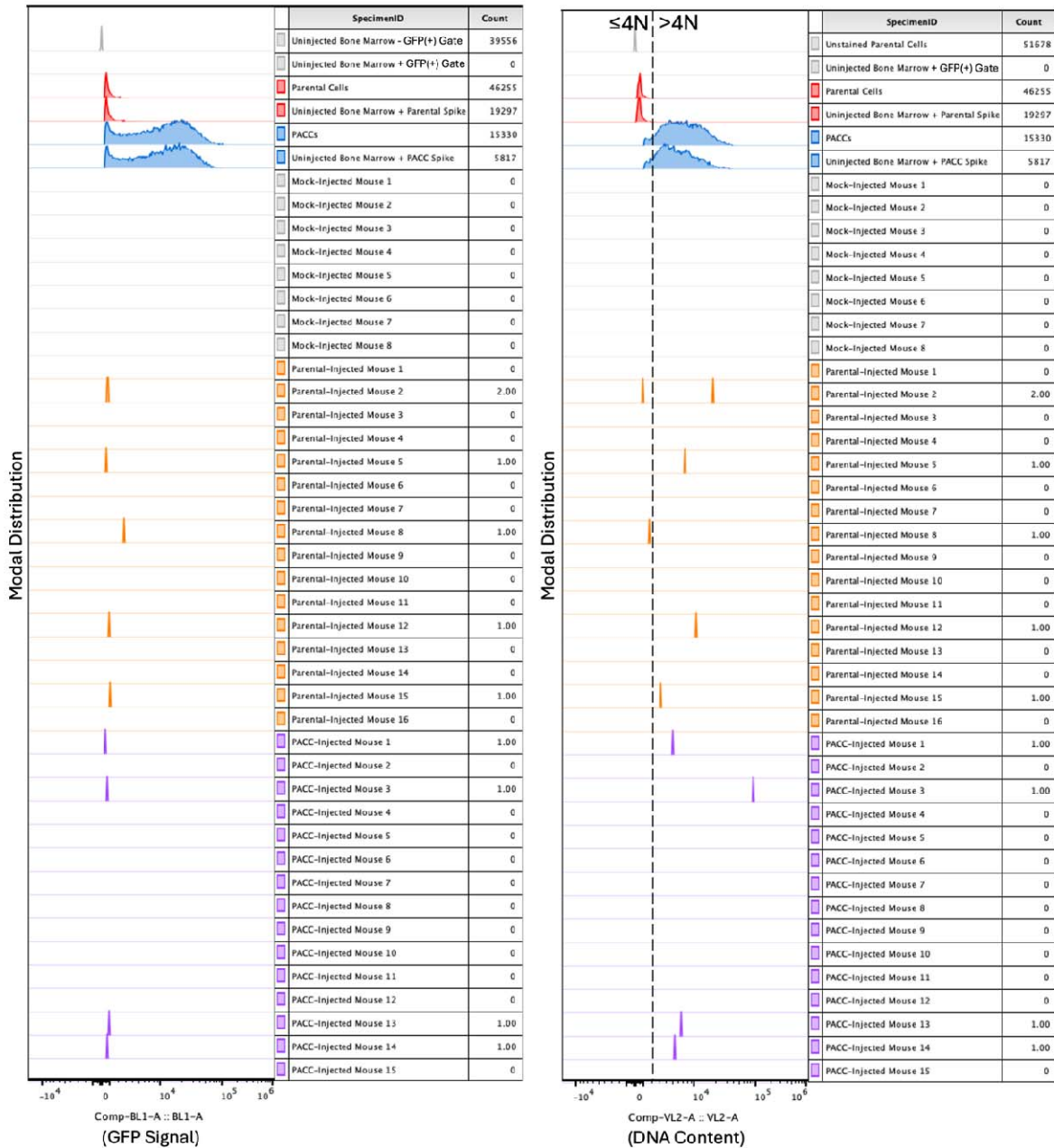


293 **Supplemental Figure S3:**

294 Size-matched, subcutaneous injection of PC3-GFP-Luc parental population vs.  
 295 PACC-enriched population: A) Raw cytometric data reporting GFP+ signal across all  
 296 blood samples. B) Raw cytometric data reporting DNA content of GFP+ cells across all  
 297 blood samples.

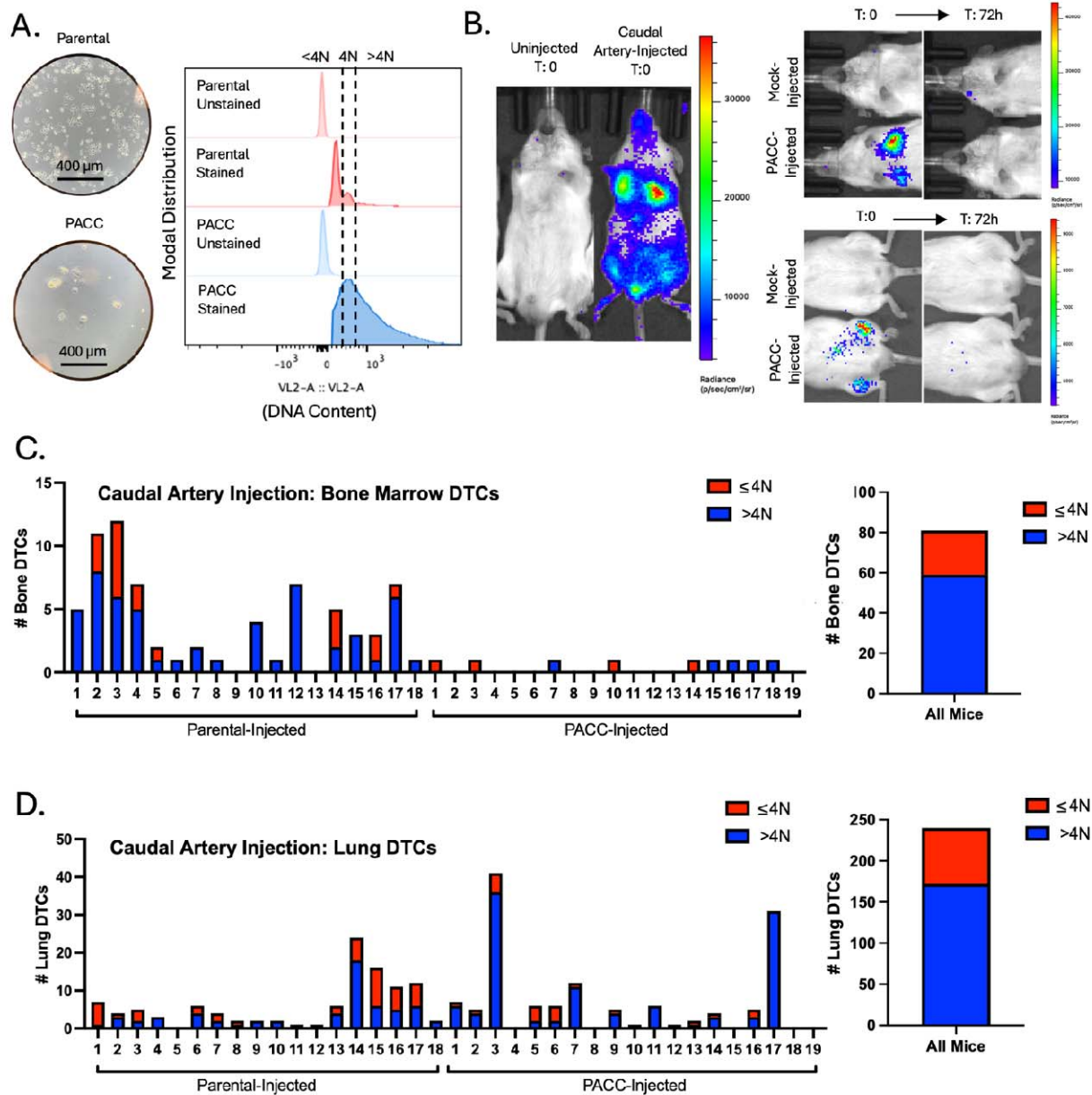
**A. Size-Matched Subcutaneous Tumor: Bone DTCs**

**B. Size-Matched Subcutaneous Tumor: Bone DTCs**



298 **Supplemental Figure S4:**

299 Size-matched, subcutaneous injection of PC3-GFP-Luc parental population vs.  
 300 PACC-enriched population: A) Raw cytometric data reporting GFP+ signal across all  
 301 bone marrow samples. B) Raw cytometric data reporting DNA content of GFP+ cells  
 302 across all bone marrow samples.  
 303

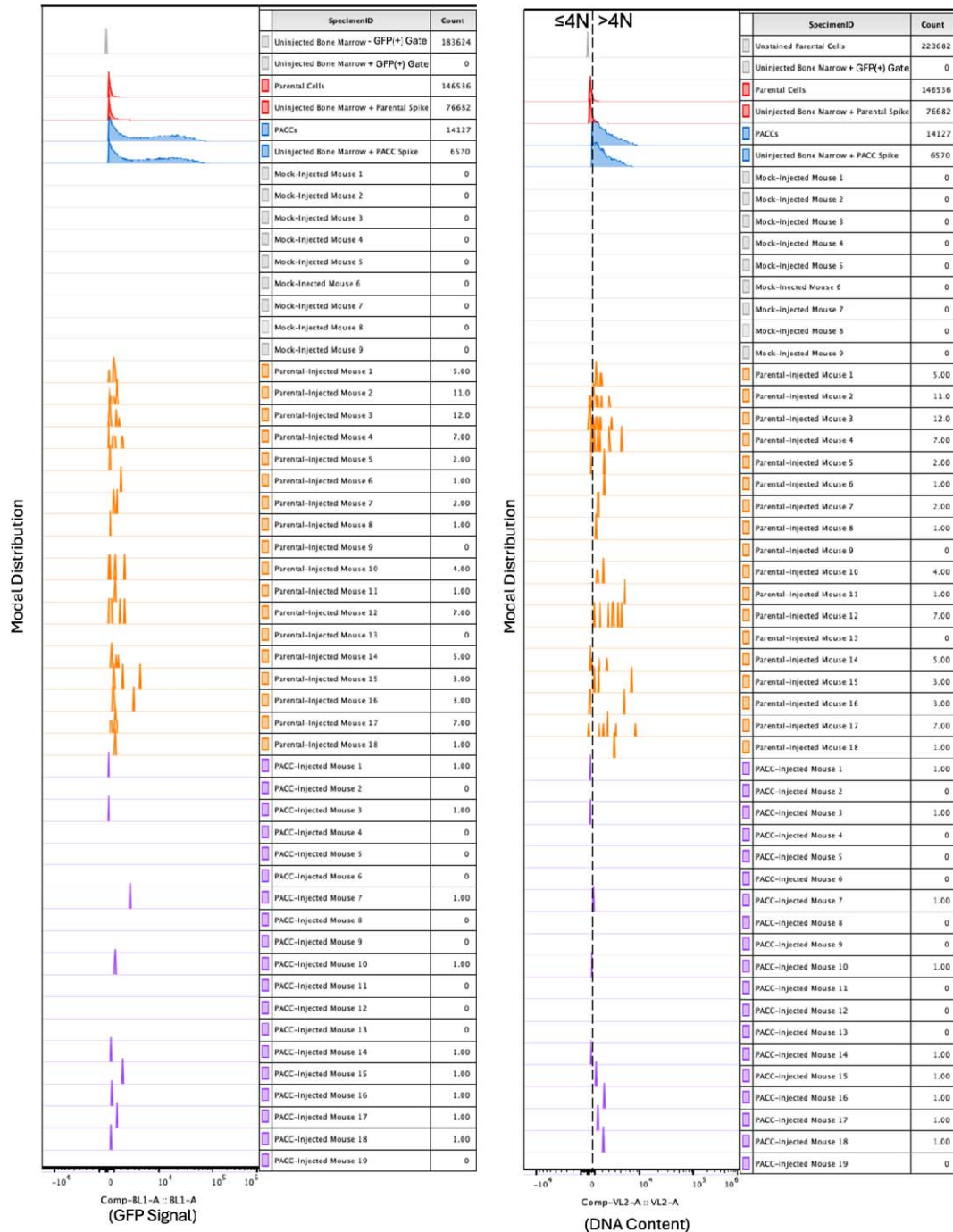


304 **Figure 3:**

305 Caudal Artery injection of PC3-GFP-Luc parental population vs. PACC-enriched  
 306 population: A) Light microscopy photos and flow-cytometric ploidy analysis of injected  
 307 cells per injection group. B) Representative BLI images capturing the cellular distribution  
 308 and signal intensity immediately following caudal artery injection and 72 hours following  
 309 caudal artery injection. C) Enumeration of DTCs sourced from the bone marrow of each  
 310 animal and quantification of %  $>4N$  DTCs vs.  $\leq 4N$  DTCs. E) Enumeration of DTCs  
 311 sourced from the lung tissue of each animal and quantification of %  $>4N$  DTCs vs.  $\leq 4N$   
 312 DTCs.

**A. Caudal Artery Injections: Bone Marrow DTCs**

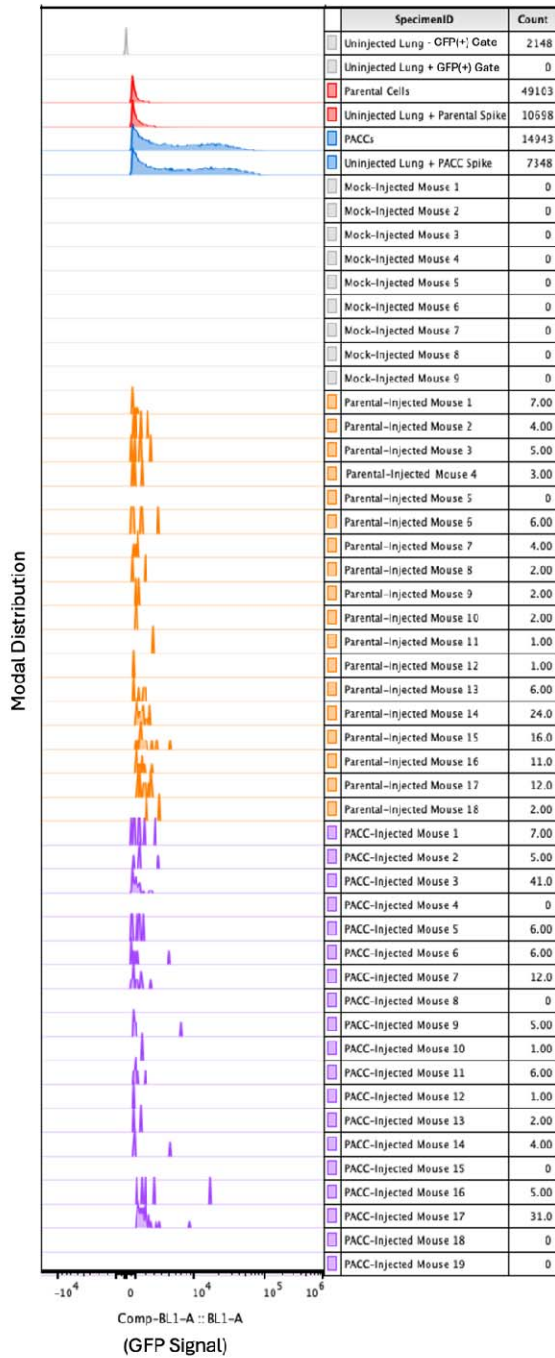
**B. Caudal Artery Injections: Bone Marrow DTCs**



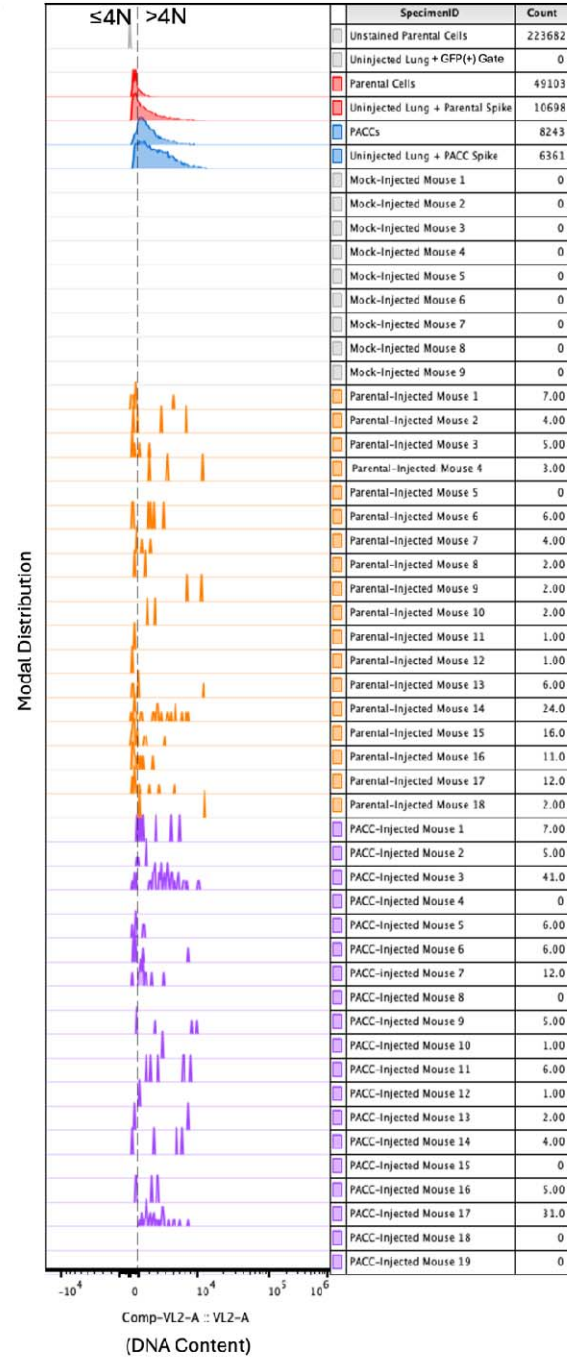
314 **Supplemental Figure S5:**

315 Caudal Artery injection of PC3-GFP-Luc parental population vs. PACC-enriched  
 316 population: A) Raw cytometric data reporting GFP+ signal across all bone marrow  
 317 samples. B) Raw cytometric data reporting DNA content of GFP+ cells across all bone  
 318 marrow samples.

**A. Caudal Artery Injections: Lung DTCs**



**B. Caudal Artery Injections: Lung DTCs**

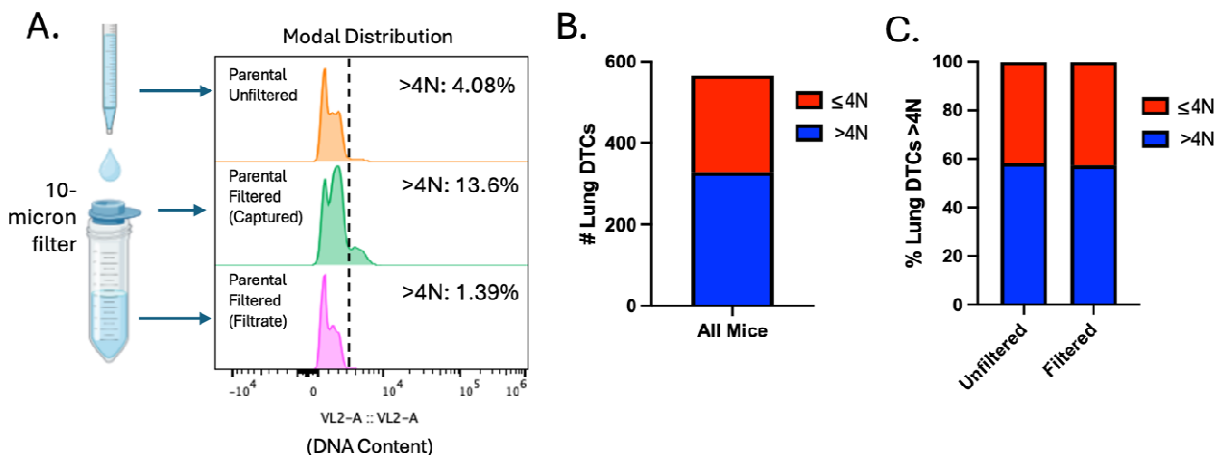


320 **Supplemental Figure S6:**

321 Caudal Artery injection of PC3-GFP-Luc parental population vs. PACC-enriched  
 322 population: A) Raw cytometric data reporting GFP+ signal across all lung tissue  
 323 samples. B) Raw cytometric data reporting DNA content of GFP+ cells across all lung  
 324 tissue samples.

325 PACCs can be found at a low baseline level (5%) in parental populations of the  
326 PC3 cell line and are generally thought to reflect the stress inherent to cell culturing.  
327 Therefore, it is possible that PACC-state DTCs recovered from parental-injected mice  
328 result from selection of pre-existing PACCs in the parental population and reflect the  
329 increased metastatic risk of cells in the PACC state. Alternatively, it is possible that  
330 stress experienced during the metastatic process induced nonPACCs in the parental  
331 population to access the PACC state *in vivo*. To investigate the source of the PACC-  
332 state DTCs recovered from parental-injected mice, we performed a tail vein experiment  
333 comparing a population of parental cells (inherently containing a small percentage of  
334 PACCs) to a population of nonPACC enriched cells generated by size-filtering a  
335 parental population through a 10-micron filter to remove PACCs. Mice were injected  
336 with either unfiltered (parental) cells or filtered (nonPACC-enriched) cells confirmed to  
337 contain fewer cells of increased ploidy (Supplemental Figure S7A). After 72 hours, lung  
338 tissues were collected and analyzed for DTCs. Across all mice, 566 DTCs were  
339 recovered, 328 of which were in the PACC state (58%). This is consistent with our  
340 previous findings (Supplemental Figure S7B). When comparing the proportion of lung  
341 DTCs in the PACC state between the two injection groups, we found no difference  
342 (unfiltered: 58% vs. filtered: 57%) (Supplemental Figure S7C). These data show that a  
343 reduction in the percentage of baseline PACCs present in the parental population does  
344 not change the percentage of PACCs present among recovered DTCs, suggesting a  
345 possibility that nonPACCs in the parental population may access the PACC state *in*  
346 *vivo*.

347 **Supplemental Figure S7:**

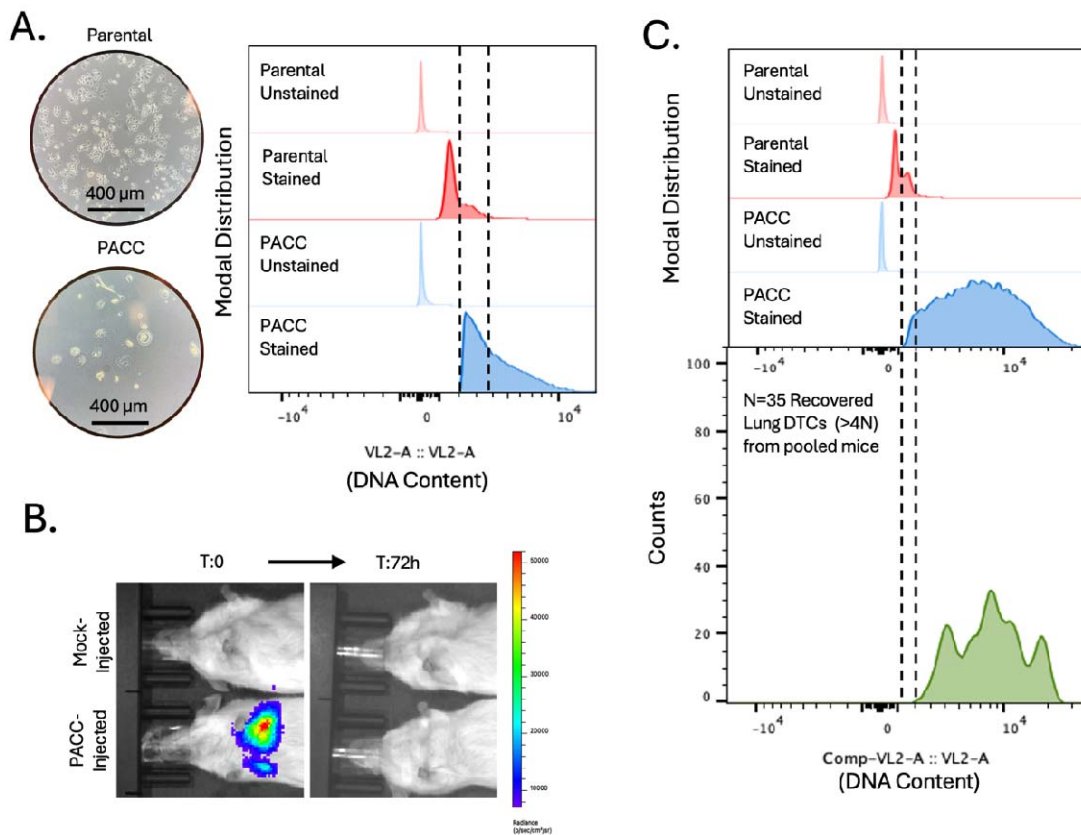


348 Tail Vein injection of PC3-GFP-Luc parental population vs. PACC-depleted  
349 parental population: A) Flow-cytometric ploidy analysis of injected cells per injection  
350 group. B) Proportion of lung DTCs with  $>4N$  DNA content across all experimental mice.  
351 C) Comparative proportions of lung DTCs with  $>4N$  DNA content between two injection  
352 groups.

353  
354 **PACCs are capable of colonization following a period of dormancy:**



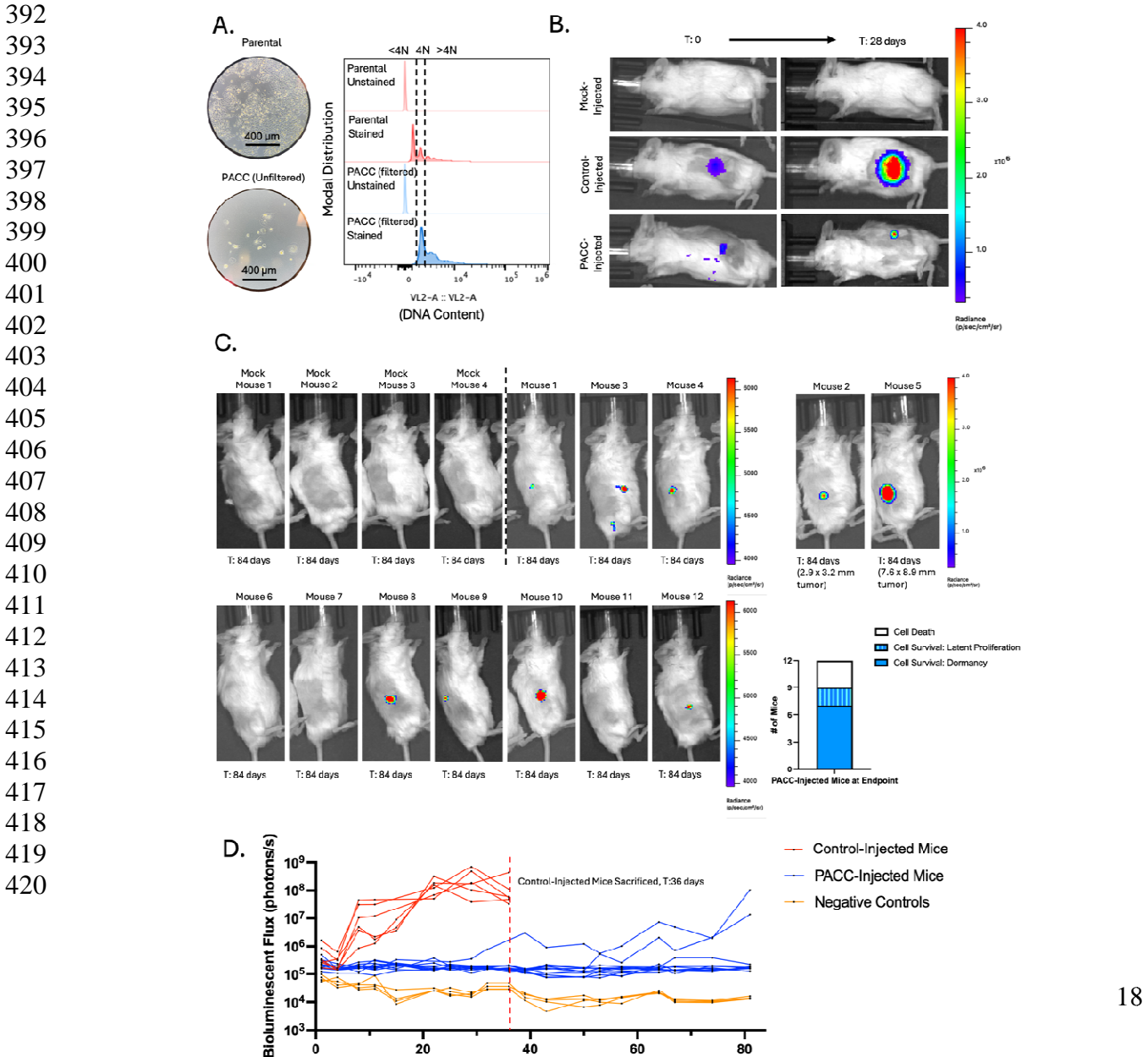
355 Clinically relevant metastatic potential requires colonization capacity. *In vitro*,  
356 cells induced to enter the PACC state become transiently nonproliferative, existing in a  
357 nondividing state. It has been observed that PACCs can survive in this state for months,  
358 a phenomenon compatible with that of metastatic tumor cell dormancy. Following a  
359 period of nonproliferative dormancy, some cells within the *in vitro* PACC-induced  
360 population return to a proliferative mitotic cell cycle, consistent with latent metastatic  
361 outgrowth frequently observed in human patients. To initially test the short-term survival  
362 status of PACCs when introduced *in vivo*, PACC-enriched cells were injected into the  
363 tail-vein of mice (Supplemental Figure S8A). The lungs were analyzed for surviving  
364 DTCs in the PACC state after 21 days (Supplemental Figure S8B). After pooling mice  
365 together, 35 DTCs in the PACC state were found still surviving in lung tissue  
366 (Supplemental Figure S8C).



368 **Supplemental Figure S8:**

369 Tail Vein injection of PC3-GFP-Luc parental population vs. PACC-enriched  
370 population: A) Light microscopy photos and flow-cytometric ploidy analysis of injected  
371 cells per injection group. B) Representative BLI images capturing the cellular distribution  
372 and signal intensity immediately following tail vein injection and 3 days following tail vein  
373 injection. C) Raw cytometric data reporting the presence of >4N Lung DTCs in a pooled  
374 sample 21 days following PACC injection.

375 Satisfied that PACCs do not immediately re-enter a proliferative cell cycle nor  
 376 immediately die when introduced *in vivo*, we sought to understand the long-term  
 377 survival and growth kinetics of PACCs *in vivo*. Mice were subcutaneously injected with  
 378 either a population of parental cells (serving as a positive control) or a population of size  
 379 filtered PACCs and monitored for 12 weeks using bioluminescent imaging (BLI). The  
 380 size filtered PACC population was confirmed to contain only cells of at least 4N or  
 381 greater ploidy. (Figure 4A). Within 4 weeks, 6/6 positive control mice developed  
 382 appreciable tumors and showed the expected marked increase in BLI flux. At that time,  
 383 0/12 PACC-injected mice presented with palpable tumors, but BLI showed evidence of  
 384 tumor cell survival at injection site (Figure 4B). Positive control mice reached ethical  
 385 tumor burden and were euthanized 6 weeks post-injection. PACC-injected mice were  
 386 monitored for an additional 6 weeks before they were euthanized. At experimental-  
 387 endpoint, all PACC-injected mice showed greater levels of BLI flux than negative  
 388 controls. 7/12 PACC-injected mice showed BLI evidence of nonproliferative tumor cell  
 389 survival localized to the injection site, and an additional 2/12 PACC-injected mice had  
 390 developed slow-growing palpable subcutaneous tumors following a latent dormancy  
 391 phase (Figure 4C, 4D).



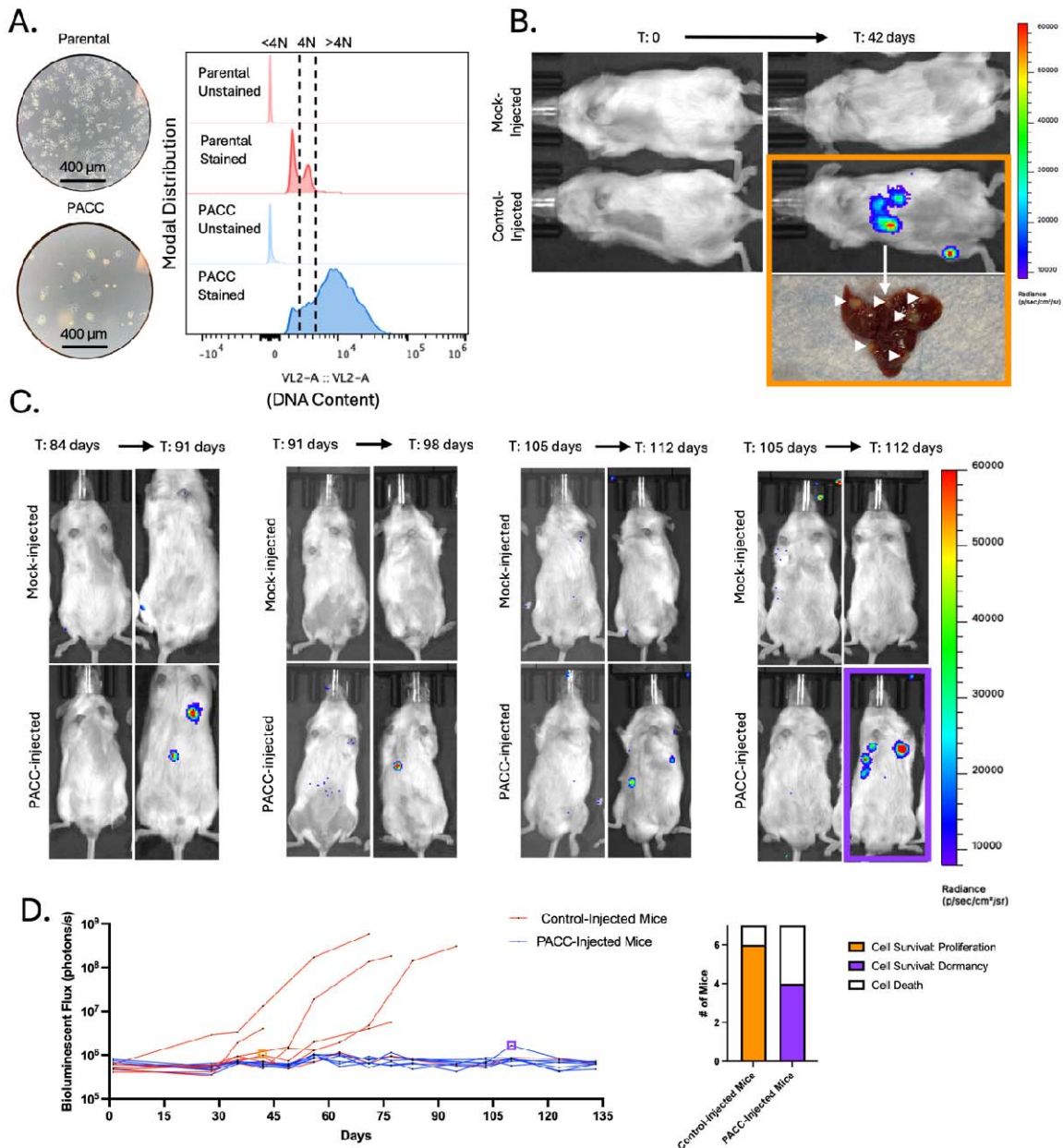
421  
422  
423  
424  
425  
426  
427  
428  
429  
430  
431  
432  
433  
434  
435  
436  
437  
438  
439  
440

441 **Figure 4:**

442 Subcutaneous injection of PC3-Luc parental population vs. size filtered PACC  
443 population: A) Light microscopy photos and flow-cytometric ploidy analysis of injected  
444 cells per injection group. B) Representative BLI images capturing the cellular distribution  
445 and signal intensity immediately following subcutaneous injection and 28 days following  
446 subcutaneous injection. C) BLI images of 4 mock-injected and 12 PACC-injected mice  
447 82 days following subcutaneous injection. Note the different scale for Mouse 2 and  
448 Mouse 5. Quantification of the status of injected cells across all 12 PACC-injected mice  
449 at experimental endpoint. D) Weekly BLI flux of all experimental mice over 84 days.

450

451 We next used an intracardiac injection model to test the dormancy and  
452 colonization kinetics of PACCs in a metastasis-relevant context (i.e. following survival in  
453 the circulation and subsequent extravasation). Mice were injected directly into the left  
454 ventricle with either a population of parental cells (serving as a positive control) or a  
455 population of PACC-enriched cells confirmed to have increased ploidy at the population  
456 level (Figure 5A). Within 6 weeks, 6/7 positive control mice had evidence of liver and/or  
457 bone metastases by BLI. At that time, 0/7 PACC-injected mice showed any BLI positive  
458 lesions (Figure 5B). Positive control mice reached ethical tumor burden and were  
459 euthanized between 6 and 14 weeks. PACC-injected mice were monitored for an  
460 additional 5 weeks. By experimental endpoint, 4/7 PACC-injected mice had showed  
461 evidence of liver metastases by BLI, but none of these metastases reached a BLI flux  
462 threshold indicative of rapidly progressive disease (Figure 5C, 5D). Taken together,  
463 these data indicate that PACCs are capable of both i) long-term *in vivo* survival in a  
464 nonproliferative state and ii) return to a proliferative phenotype able to seed metastatic  
465 colonization following a period of dormancy.



466  
467  
468  
469  
470  
471  
472  
473

**Figure 5:**

Intracardiac injection of PC3-GFP-Luc parental population vs. PACC-enriched population: A) Light microscopy photos and flow-cytometric ploidy analysis of injected cells per injection group. B) Representative BLI images capturing the cellular distribution and signal intensity immediately following intracardiac injection and 42 days following intracardiac injection. C) BLI images of 4 mock-injected and 4/7 PACC-injected mice that showed evidence of colonization following dormancy between 91- and 112-days post intracardiac injection. D) Weekly BLI flux of all experimental mice over 135 days.

474 Quantification of the status of injected cells across all 7 PACC-injected mice at  
475 experimental endpoint.

476 **PACCs display a partial EMT phenotype:**

477 *In vitro* studies show that cells in the PACC state display enhanced metastatic  
478 phenotypes including motility, chemotaxis, and invasion (20, 21). The present work  
479 shows that most CTCs and DTCs recovered across various metastatic models are in  
480 the PACC state, supporting the hypothesis that PACCs promote a tumor's metastatic  
481 potential through cell-intrinsic metastatic competency. In the past decade, it has been  
482 increasingly reported that metastatic competency relies heavily on a partial-Epithelial-to-  
483 Mesenchymal-Transition (pEMT) phenotype. pEMT (also called hybrid-EMT and mixed-  
484 EMT, among other similar names) is a nonbinarized variant of the canonically mutually  
485 exclusive epithelial vs. mesenchymal phenotypes that is characterized by co-expression  
486 of proteins typically associated with only one or the other. Using the PC3 prostate  
487 cancer cell line, we found that at the RNA level, PACCs show an increase in *ZEB1*,  
488 *VIM*, and *CLDN1* expression and no difference in *SNAI1*, *SNAI2*, *TWIST1*, *CDH2*,  
489 *CDH1*, or *EPCAM* expression (Figure 6A). At the protein level, PACCs show an  
490 increase in *VIM*, *CDH2*, *CLDN1*, and *CDH1* expression, a decrease in *SNAI1*, *SNAI2*,  
491 and *EPCAM* expression, and no change in low-level *TWIST1* expression (Figure 6B).  
492 High co-expression of *VIM* (a classic mesenchymal marker) and *CLDN1* (a known  
493 epithelial marker) in PACCs indicate a pEMT phenotype. Absence of inverse expression  
494 between PACC *CDH2* (a classic mesenchymal marker) and PACC *CDH1* (a classic  
495 epithelial marker) also supports a PACC-specific pEMT phenotype (Figure 6C).

496 To evaluate the pEMT status of metastatic PACCs in a clinical context, we  
497 stained cancer cells in the bone marrow isolated from prostate cancer patients with a  
498 DNA content dye, a cocktail of epithelial-specific markers, and Vimentin. Cells with 4x-  
499 greater-than-average nuclear area were deemed PACCs. Single-cell copy number  
500 analysis confirmed that the PACCs were tumor-derived (Figure 6D). 34 of 44 patients  
501 were found to have PACC cancer cells. Of those 34, 6 patients were found to have  
502 pEMT PACC cancer cells positive for both pan-Epithelial (including *EPCAM*) and *VIM*  
503 stains (Representative images: Figure 6E). These data support our *in vitro* observations  
504 of PACC-specific pEMT in metastatic prostate cancer patients and provide a plausible  
505 mechanism for increased metastatic competency among cells in the PACC state.  
506

507  
508  
509  
510  
511  
512  
513  
514  
515  
516  
517  
518  
519  
520  
521  
522  
523  
524  
525  
526  
527  
528  
529  
530  
531  
532  
533  
534  
535  
536  
537  
538  
539  
540  
541

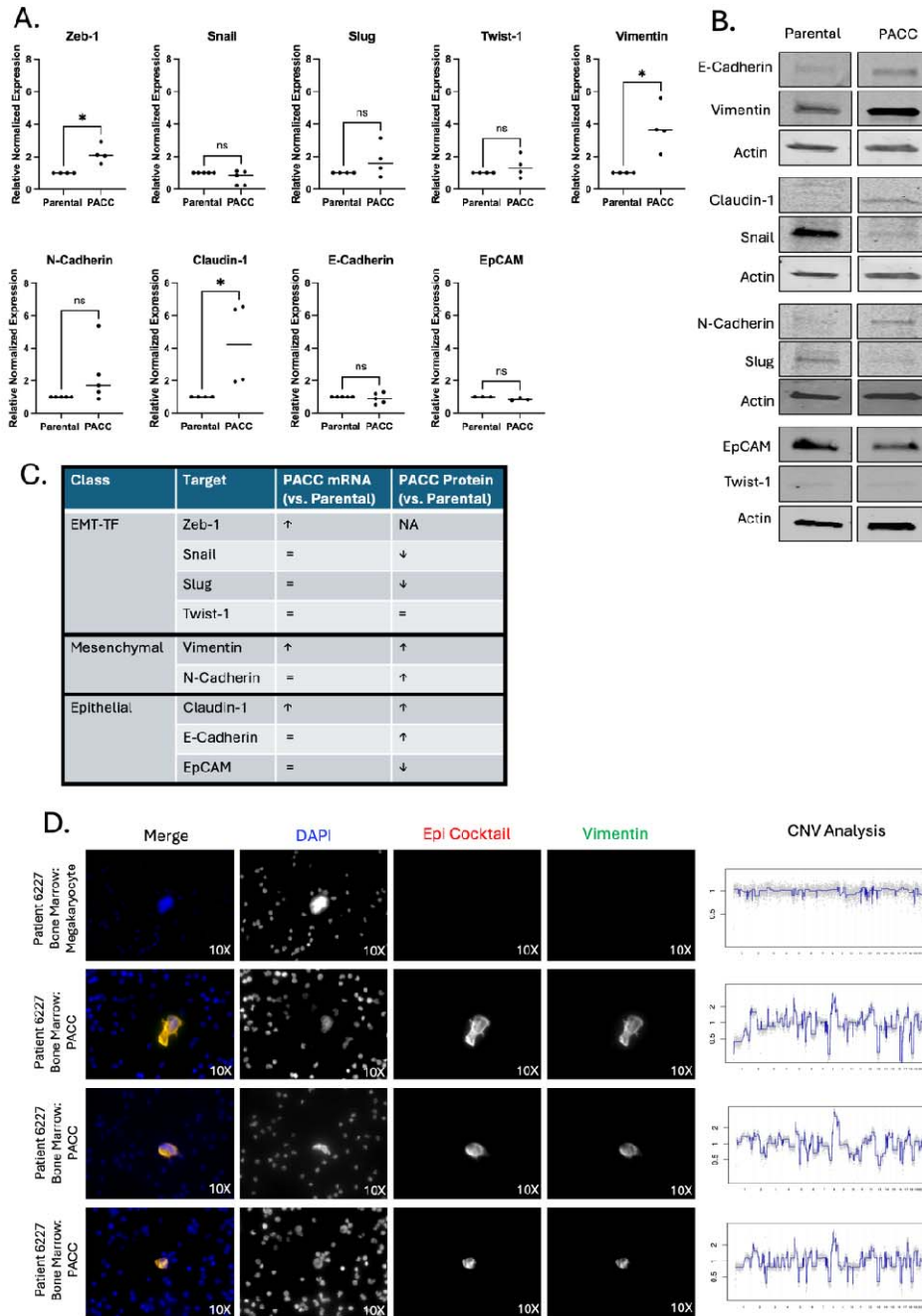
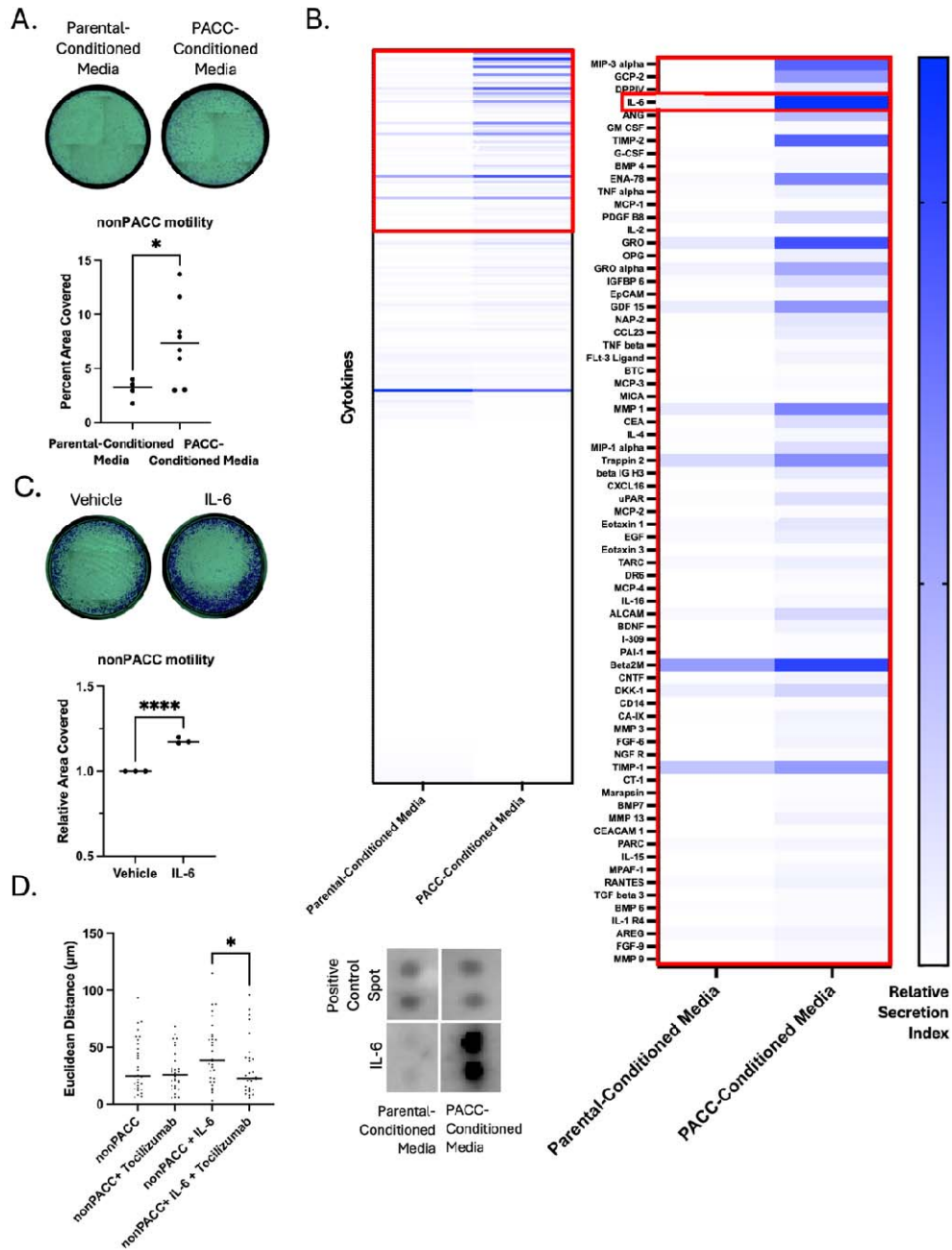


**Figure 6:**

543 PACCs have a pEMT phenotype: A) RNA expression of a panel of EMT markers  
544 by RTqPCR in a PC3-Luc parental population vs. size filtered PACC population. B)  
545 Protein expression a panel of EMT markers by Western blot in a PC3-Luc parental  
546 population vs. size filtered PACC population, where each biological replicate reported is  
547 an average of three technical replicates. C) Summary table of RNA and protein  
548 expression. D) Representative immunofluorescent images of PACCs identified as DTCs  
549 in the bone marrow of a metastatic prostate cancer patient, stained for DAPI, an  
550 Epithelial-origin cocktail, and VIM. CNV analysis of the corresponding single cell.  
551 **PACCs have a pro-metastatic secretory profile:**

552 In addition to the hypothesis that PACCs promote a tumor's metastatic potential  
553 because PACCs themselves are more metastatic, PACCs might otherwise promote a  
554 primary tumor's metastatic potential by increasing the metastatic phenotype of  
555 surrounding tumor cells. To test this alternative model, we evaluated the motility  
556 phenotype of nonPACC cells cultured in PACC-conditioned media compared to control  
557 parental cell-conditioned media. We found that PACC-conditioned media increases  
558 nonPACC motility by two common motility assays (Figure 7A, Supplemental Figure  
559 S9A), which was not accompanied by an increased transcriptional EMT phenotype  
560 (Supplemental Figure S9B).

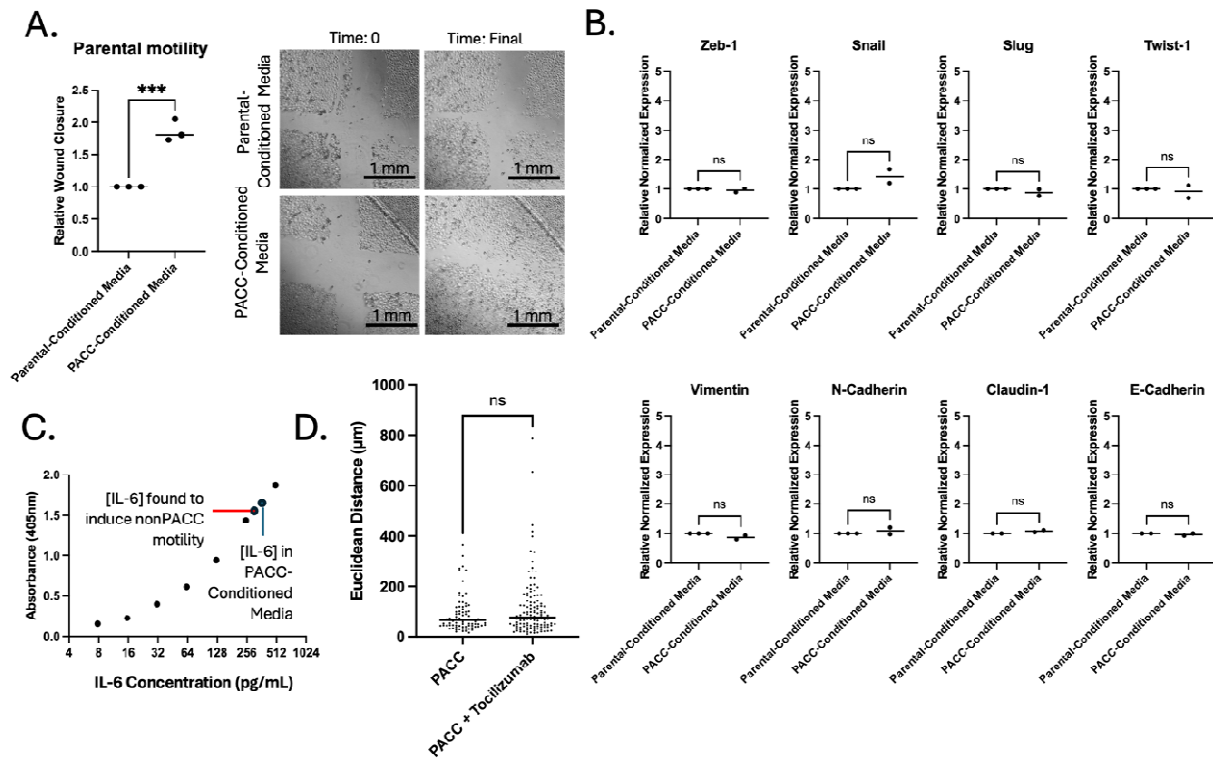
561 We performed a cytokine array on parental cell-conditioned media and PACC-  
562 conditioned media to identify abundant cytokines differentially secreted by PACCs. IL6  
563 was the strongest candidate for further study (Figure 7B). We measured the  
564 concentration of IL6 in PACC-Conditioned Media (Supplemental Figure S9C) and found  
565 that a similar concentration was sufficient to produce increased motility in nonPACCs  
566 (Figure 7C). This increased motility phenotype was abrogated by inhibition of the IL6  
567 Receptor (IL6R) via addition of Tocilizumab (Figure 7D). We and others have previously  
568 published the PACCs are more motile than nonPACCs (20, 21). To rule out the  
569 possibility that increased PACC motility is the result of autocrine-acting IL6, we applied  
570 Tocilizumab to PACC samples and observed no change in PACC motility  
571 (Supplemental Figure S9D). These data suggest that in addition to cell-autonomous  
572 pro-metastatic effects, PACCs contribute to a tumor microenvironment that promotes  
573 pro-metastatic phenotype in nonPACC tumor cells.  
574



575 **Figure 7:**

576 PACCs have a pro-metastatic secretory profile: A) Transwell assay to measure  
 577 the differential motility of a PC3-Luc population exposed to parental-conditioned media  
 578 vs. PACC-conditioned media, where each reported biological replicate is an average of  
 579 two technical replicates. B) Cytokine array to measure the relative abundance of 274  
 580 cytokines of interest in parental-conditioned media vs. PACC-conditioned media. C)  
 581 Transwell assay to measure the effect of addition of recombinant IL6 on the motility of a  
 582 PC3-Luc population. D) Single cell tracking to measure the effects of addition of  
 583 recombinant IL6 and/or Tocilizumab on the motility of a PC3-Luc population.





584 **Supplemental Figure S9:**

585 PACCs have a pro-metastatic secretory profile: A) Wound-healing assay to

586 measure the differential motility of a PC3-Luc population exposed to parental-

587 conditioned media vs. PACC-conditioned media, where each reported biological

588 replicate is an average of two technical replicates. B) RNA expression of a panel of

589 EMT markers by RTqPCR in a PC3-Luc parental population exposed to parental-

590 conditioned media vs. PACC-conditioned media, where each biological replicate reported

591 is an average of three technical replicates. C) Elisa assay to measure the concentration

592 of IL6 in PACC conditioned media. D) Single cell tracking to measure the effects of

593 addition of Tocilizumab on the motility of a PACCs.

594

595

596

597

598

599

600

601

602

603

604

605

606

607 **III. Discussion:**

608

609 Our recent study demonstrating the clinical relevance of cells in the PACC state  
610 as reliable predictors of the risk of prostate cancer recurrence (27) raised important  
611 questions about the roles that PACCs may play in metastatic progression. For example,  
612 accession of the PACC state may increase intrinsic pro-metastatic features, making  
613 PACCs more metastatically competent than their nonPACC counterparts. Alternatively,  
614 PACCs may increase the metastatic competency of nearby nonPACCs via a paracrine-  
615 functioning pro-metastatic phenotype. Or perhaps PACCs are merely uninvolved “third-  
616 party” cells incidentally produced by an unknown stimulus that itself is driving metastatic  
617 risk via an otherwise unrelated mechanism. Here, we sought to test for a direct  
618 causative link between PACC presence and metastatic propensity. We tested for the  
619 presence of PACCs throughout various steps – and therefore locations – of the  
620 metastatic cascade using distinct metastatic mouse models.

621 When testing the blood for metastatic cells capable of invading, intravasating,  
622 and then surviving in the circulation, we found that 75% of recovered CTCs were in the  
623 PACC state (27/36 CTCs). When testing the bone marrow for metastatic cells capable  
624 of invading, intravasating, surviving, and then extravasating, we found that 77% of  
625 recovered DTCs were in the PACC state (14/18 DTCs). It was pertinent to test both  
626 time-matched and size-matched subcutaneous models to account for any potential  
627 effects that the differing growth kinetics of the two injections groups might have had on  
628 the initiation of the angiogenic switch. Appropriately, an increased number of total CTCs  
629 and DTCs were recovered in the size-based experiment that at endpoint had larger  
630 primary tumors than the time-based experiment. We did not consistently find that  
631 PACC-injected mice produced a larger number of metastasizing cells. Analysis of the  
632 proportion of PACCs within the tumors of each injection group at experimental endpoint  
633 offered a potential explanation: the initial difference between the proportions of PACCs  
634 within each injected population (less than 5% PACCs among parental populations, but  
635 over 50% among PACC-enriched populations) equilibrated within 6 weeks. A decrease  
636 in PACC proportion over time in the PACC-enriched tumors could be caused by a  
637 delayed return to mitotic cell cycle among PACCs, or a presence of a small number of  
638 mitotic nonPACCs in the injection population. An increase in PACC proportion over time  
639 in the parental population could be caused by accumulation of tumor  
640 microenvironmental stressors *in vivo* that initiate PACC state entry as has been  
641 previously reported (18, 29, 30).

642 The similarity between the proportions of PACCs found among the recovered  
643 CTCs and the recovered DTCs (75% vs 77%) in the subcutaneous tumor models does  
644 not adequately support a conclusion of increased extravasation potential among cells in  
645 the PACC state. To specifically test for increased extravasation potential among  
646 PACCs, we used a caudal artery injection model that allowed for analysis of bone  
647 marrow, the most common site of prostate metastasis in patients. When testing the  
648 bone marrow for metastatic cells capable of extravasation, we found that 73% of  
649 recovered DTCs were in the PACC state (59/81 DTCs). When testing the lung for  
650 metastatic cells capable of extravasation, we found that 84% of recovered DTCs were in  
651 the PACC state (111/132 DTCs). This data indicates that cells in the PACC state have  
652 increased extravasation potential compared to nonPACCs. We and others have

653 previously published that PACCs demonstrate both persistent chemotactic-driven  
654 motility and functional deformability, phenotypes which may explain their increased  
655 ability to extravasate (20, 21). An alternative hypothesis supposes that extravasated  
656 nonPACCs entered the PACC state after entering secondary organ tissue owing to the  
657 inherent stressors of that organ site. When comparing the portion of PACCs found  
658 among total DTCs in the lungs of animals injected with parental populations with low-  
659 level baseline PACCs vs. a PACC-depleted population, we found that reduction of  
660 baseline PACCs present does not change the percentage of PACCs present among  
661 recovered DTCs. This data suggests that it is possible that stress experienced during  
662 the metastatic process may induce nonPACCs to access the PACC state *in vivo*, but  
663 further study is necessary.

664 Interestingly, in the caudal-artery model, most of the bone marrow DTCs were  
665 sourced from parental-injected mice (though the majority of those DTCs were in the  
666 PACC state), but the majority of lung DTCs were sourced from PACC-injected mice.  
667 This difference may represent biologically interesting differences in tissue-specific  
668 extravasation-barriers. For example, potential size or biophysical rigidity restrictions in  
669 the bone marrow may select for cells in the PACC state on the smaller end of what is  
670 known to be a heterogenous spectrum: the number of endocycles is inherently linked to  
671 the size of a PACC's nucleus and cell body. Notably, baseline PACCs found in parental  
672 populations are frequently smaller than PACCs found in chemotherapy induced  
673 populations. It is possible, therefore, that bone-specific environmental pressure selects  
674 for extravasation of small PACCs, which are disproportionately found in parental  
675 populations.

676 Presence of CTCs and DTCs alone is not sufficient to claim complete metastatic  
677 competency; evidence of functional colonization is also needed. Multiple *in vitro* studies  
678 have reported on the latent depolyploidization (also called ploidy reversal or ploidy  
679 reduction) of cells in the PACC state following long stints of survival without cell division  
680 (31-35). The progeny of PACCs appear to be of typical cancer cell size and genomic  
681 content and display a typical mitotic cell cycle. We used two models to specifically test  
682 the dormancy and colonization potential of PACCs *in vivo*. In both settings, the PACC  
683 state life cycle closely followed what has been observed *in vitro*. 12 weeks following  
684 subcutaneous injection of size filtered PACCs (to remove any infiltrating mitotic  
685 nonPACC cells), 7/12 mice showed survival of nonproliferative PACCs at the injection  
686 site, and 2/12 mice showed delayed tumor establishment followed by slow proliferation,  
687 indicative of an *in vivo* depolyploidization event. By 19 weeks following intracardiac  
688 injection of PACCs, 4/7 mice had established, presumably proliferative, metastatic  
689 lesions.

690 Taken together, our *in vivo* data provides strong evidence of a causative  
691 relationship between PACCs and metastasis. Next, we sought to establish a preliminary  
692 mechanism underlying this pro-metastatic phenotype. In the past decade, there has  
693 been a notable shift away from a binary and mutually exclusive Epithelial vs.  
694 Mesenchymal phenotype. Instead, researchers have begun to appreciate the existence  
695 – and importance – of pEMT phenotypes. In fact, many groups have reported that cells  
696 with pEMT expression profiles display increased metastatic competency (36-39),  
697 perhaps owing to the needs of successfully metastatic cells to have motility programs  
698 that mesenchymal cells provide and the proliferative programs that epithelial cells

699 provide. Our RNA and protein analysis of cells in the PACC state revealed a clear  
700 pEMT pattern, most strongly supported by simultaneous expression of *CDH1* and *VIM*.  
701 Notably, others have also reported pEMT phenotypes in PACCs (40). Analysis of bone  
702 marrow DTCs from patients with prostate cancer supported our *in vitro* findings: patient  
703 bone marrow contained PACCs co-expressing pan-Epithelial markers (including  
704 EPCAM) and *VIM* at the protein level.

705 To test for a potentially indirect mechanistic link, we turned to the literature citing  
706 the similarities between what we have termed cells in the PACC state and what others  
707 have termed therapy-induced senescent cells (41-45). The therapy-induced senescent  
708 cell literature defines this cell type as one arising in response to treatment and  
709 characterized, among other features, by a transient pause in cell cycle. Though therapy-  
710 induced senescent cells depart from classically terminal senescent cells in several  
711 ways, they have been reported to share the senescence-associated secretory  
712 phenotype (SASP). Most notably, the SASP has been reported to contribute to a more  
713 pro-metastatic tumor microenvironment (46, 47). Accordingly, we thought it possible  
714 PACCs might promote the metastatic phenotype of surrounding nonPACC tumor cells  
715 by contributing to a pro-metastatic tumor microenvironment. We found that PACCs  
716 produce a SASP-like secretory profile rich in MIP3-alpha, GCP-2, DPPIV, IL-6, GM-  
717 CSF, G-CSF, ENA-78, TNF alpha, MCP-1, IL-2, and GRO, among many others (For  
718 clarity, cytokine annotations used here are consistent with those on the product sheet).  
719 Furthermore, this co-culture with PACC conditioned media increased the motility of  
720 nonPACC cells. A validation of the most differentially secreted cytokine, IL6, showed  
721 that it was sufficient to induce motility induction in a PACC-to-nonPACC paracrine, but  
722 not a PACC-to-PACC autocrine, setting. We are not the first to find an IL6 rich PACC-  
723 secretome (48), and of note, the motility-inducing nature of IL6 has been previously  
724 published in other contexts (49).

725 The PACC state represents an emerging area of cancer research committed to  
726 understanding the adaptive phenotypic potential of cancer cells. It has been well  
727 established that treatment of cancer with chemotherapeutic agents inevitably leads to  
728 the eventual rise of treatment-resistant disease. Though outside the scope of this  
729 manuscript, it has been repeatedly shown that cells in the PACC state are broadly  
730 resistant to a wide swath of anti-cancer agents (8, 10, 13, 43, 48, 50, 51). In addition to  
731 chemotherapy-induced resistance, evidence has begun to suggest that cancers treated  
732 with chemotherapeutics are prone to become more metastatic. For example, emerging  
733 evidence show that chemotherapy induces cancer-cell intrinsic changes such as  
734 upregulation of anti-apoptotic genes and increased migration (52). When tested in mice  
735 using spontaneously metastatic orthotopic breast models, it was found that paclitaxel  
736 increased metastasis despite decreases in tumor burden (52). Karagiannis et. al,  
737 demonstrated that this observation holds true in the patient setting: clinically validated  
738 prognostic markers of metastasis in breast cancer patients were increased in patients  
739 who received neoadjuvant paclitaxel after doxorubicin plus cyclophosphamide (53).  
740 Considering that nearly all anti-cancer agents tested have shown to induce cells into the  
741 PACC state, our data demonstrating the increased metastatic competency of PACCs  
742 positions the PACC state as an important unforeseen ramification of neoadjuvant  
743 regimens that may help to explain clinical correlations between chemotherapy and  
744 metastatic progression.

## 745 **IV. Materials and Methodology:**

746

### 747 **Cell Culture:**

748 Experiments were performed using either the PC3-Luc prostate cancer cell line or  
749 the PC3-GFP-Luc prostate cancer cell line generated as previously described (28). All  
750 cells were cultured with RPMI 1640 media containing L-glutamine and phenol red  
751 additives (Gibco) and further supplemented with 10% Premium Grade Fetal Bovine  
752 Serum (Avantor Seradigm) and 1% 5000U/mL Penicillin-Streptomycin antibiotic (Gibco)  
753 at 37 degrees Celsius and in 5% CO<sub>2</sub>. Cells were routinely lifted using TrypLE (Gibco)  
754 following a single PBS wash (Gibco). Cells were STR-profile authenticated and tested  
755 for *mycoplasma* contamination biannually (Genetica).

756

### 757 **PACC induction:**

758 Cells were induced to enter the PACC state as previously described (11, 21).  
759 Briefly, 625,000 PC3 cells/T75 flask (scaled for appropriately for larger tissue culture  
760 vessels) were treated with 6 μM Cisplatin (Millipore Sigma) resuspended in sterile PBS  
761 supplemented with 140mM NaCl (Sigma-Aldrich) for 72 hours. Where indicated, PC3-  
762 GFP-Luc cells were treated with 12 μM Cisplatin for 72 hours. After 72 hours, Cisplatin-  
763 treated media was removed and replaced with fresh complete media. Cells were  
764 injected (or assayed, where appropriate) 10 days after Cisplatin-treatment removal,  
765 unless indicated otherwise. When indicated, cells were filtered through a 10-micron cell  
766 strainer (PluriSelect) to either isolate or remove PACCs, which are larger in size, from  
767 the other cells in the population, as previously described (21).

768

### 769 **Animal Models:**

770 All murine protocols were approved by the Johns Hopkins Animal Care and Use  
771 Committee. Most experiments were performed using 8–12-week-old male Nod-Scid-  
772 Gamma (NSG) mice (Jackson Laboratories). Intracardiac injections were performed on  
773 6-week-old mice. Subcutaneously injected mice received a 100 uL injection of a 1:1  
774 ratio of 10 mg/mL Matrigel (Corning) to 200,000 PC3-GFP-Luc cells suspended in  
775 complete media (or a mock suspension of media alone). Caudal artery-injected mice  
776 received a 100 uL injection of 200,000 cells suspended in sterile PBS. Tail vein-injected  
777 mice received a 100 uL injection of 200,000 PC3-GFP-Luc cells suspended in sterile  
778 PBS. Intracardiac-injected mice received a 100 uL injection of 50,000 PC3-GFP-Luc  
779 cells suspended in sterile PBS into the left ventricle. Tumor progression of  
780 subcutaneously injected mice was monitored via weekly caliper measurements and  
781 tumor volume was calculated using the following formula:  $V = 0.5 * L * W^2$ . Progression  
782 of caudal artery-injected, tail vein-injected, and intracardiac-injected mice was  
783 monitored via BLI, wherein mice were injected with 100 μL of 30 mg/mL luciferin (Regis)  
784 and imaged within 15 minutes using the IVIS Spectrum BLI imager (Revity). At  
785 experimental endpoint, subcutaneous tumors were dissection, fixed in 10% Neutral  
786 Buffered Formalin (Sigma-Aldrich) for 24 hours, washed 3x 5 minutes in PBS, and  
787 embedded into paraffin blocks. 4-micron thick sections were mounted on slides, stained  
788 with Hematoxylin and Eosin, and imaged using a 40X objective.

789

### 790 **CTC and DTC Analysis:**

791 CTC and DTC detection and analysis was performed as previously described  
792 (28). CTCs were defined as GFP-positive cells identified in mouse blood by flow  
793 cytometry. 500  $\mu$ L of blood was collected via terminal tail bleed. Blood samples were  
794 individually transferred to 5 mL Eppendorf tubes and supplemented with ACK lysis  
795 buffer (Quality Biological) at a 1:4 blood:lysis buffer ratio. This solution was incubated  
796 on an end-over-end turner for 10 minutes. Following incubation, all samples were  
797 centrifuged at 1500 xg for 10 minutes at 4 degrees C. Cell pellets were resuspended in  
798 1 mL complete media and stained with 1  $\mu$ L of Vybrant DyeCycle Violet (Thermo Fisher  
799 Scientific).

800 DTCs were defined as GFP-positive cells identified in mouse hind-limb blood  
801 marrow or homogenized lung tissue by flow cytometry. Bone marrow was collected  
802 from the hind limb bones of freshly euthanized mice using a standard centrifugation  
803 protocol. Briefly, the right and left femurs and tibias of each mouse were dissected. The  
804 distal femoral epiphysial plate from each femur and the proximal tibial epiphysial plate  
805 from each tibia were removed to ensure access to red bone marrow. Bones were  
806 placed marrow-exposed side down in a 0.5 mL tube punctured with a small hole which  
807 was then nested into a 1.5 mL tube. Tubes were centrifuged at maximum speed for 30  
808 seconds to collect bone marrow into the 1.5 mL tube. All samples were resuspended in  
809 200  $\mu$ L PBS and then supplemented with 800  $\mu$ L of ACK lysis buffer. This solution was  
810 incubated on an end-over-end turner for 10 minutes. Following incubation, all samples  
811 were centrifuged at 1500 xg for 10 minutes at 4 degrees C. Cell pellets were  
812 resuspended in 3 mL complete media and stained with 15  $\mu$ L of Vybrant DyeCycle  
813 Violet.

814 To collect lung tissue, all 5 lobes of the lungs were dissected from freshly  
815 euthanized mice. Each sample was transferred to a petri dish and minced into small  
816 pieces with a fresh, straight-edged razor blade. Each sample was transferred to a 14  
817 mL round-bottom tube and suspended in 5 mL of a solution containing 250  $\mu$ L  
818 Collagenase/Hyaluronidase (Stem Cell Technologies), 375  $\mu$ L DNase I (Stem Cell  
819 Technologies) at 1 mg/mL, and 1.875 mL complete media. The samples were incubated  
820 at 37 degrees C for 20 minutes with shaking, before being pushed through a fresh 70-  
821 micron strainer placed over a 50 mL conical tube using the rubber end of a fresh 5 mL  
822 syringe plunger. 45 mL of complete media was used per sample to facilitate straining.  
823 Following straining, samples were centrifuged at 300 xg for 10 minutes at room  
824 temperature. The cell pellets were resuspended in 2 mL of ACK lysis buffer and  
825 incubated at room temperature for 3 minutes before adding 47 mL of complete media.  
826 Samples were then centrifuged at 300 xg for 10 minutes at room temperature, using a  
827 slow deceleration setting. Cell pellets were resuspended in 2 mL of complete media and  
828 stained with 10  $\mu$ L of Vybrant DyeCycle Violet.

829 The entire volume of all stained samples was run on the Attune NxT Acoustic  
830 Focusing Cytometer (Thermo Fisher Scientific) at a flow rate of 1000  $\mu$ L per minute. As  
831 previously described, it was critical to implement the following four modifications to our  
832 cytometer to accommodate analysis of cells in the PACC state: 1) The largest  
833 commercially available blocker bar was installed. 2) An alternative optical configuration  
834 was used. 3) Thresholding was performed using SSC rather than the standard FSC. 4)  
835 Area scaling factors of 0.6 were used for all lasers, rather than the standard area  
836 scaling factors. With these modifications, data was collected in the SSC, VL1-A, VL2-A,

837 and BL1-A channels. All data were analyzed using FlowJo (BD), following our  
838 previously published analysis protocol (28).

839

#### 840 **Patient bone marrow samples:**

841 Bone marrow aspirate (BM) samples were collected from castrate-resistant  
842 prostate cancer patients as previously described (54). Briefly, liquid biopsy samples  
843 were taken from participants at baseline and immediately started treatment on trial  
844 NCT01505868 which evaluated cabazitaxel with or without carboplatin. Samples were  
845 collected at MD Anderson at baseline prior to clinical trial treatment administration. The  
846 study was approved by the corresponding institutional review boards and was  
847 conducted in accordance with ethical principles founded in the Declaration of Helsinki.  
848 All patients gave written informed consent.

849

#### 850 **Patient sample processing:**

851 Samples were processed as previously described (54). In short, bone marrow  
852 samples were delivered overnight (7.5 mL) in Cell-Free DNA Blood Collection Tubing  
853 (Streck) at the clinical sites and sent to the University of Southern California for  
854 processing. Erythrocytes were lysed via ammonium chloride and the entire nucleated  
855 cell population was plated onto a specialized cell adhesion glass slide (Marienfield) at a  
856 density of 2-3 million cells per slide. Slides were stored at -80°C until use.

857

#### 858 **Immunofluorescent staining:**

859 Slides were fixed with 2% PFA for 20 minutes. Slides were then blocked with 2%  
860 BSA in PBS. Slides were then incubated overnight at 4°C with an antibody cocktail  
861 consisting of mouse IgG1/Ig2a anti-human cytokeratins (CK) 1, 4, 5, 6, 8, 10, 13, 18,  
862 and 19 (clones: C-11, PCK-26, CY-90, KS-1A3, M20, A53-B/A2, C2562, Sigma, St.  
863 Louis, MO, USA), mouse IgG1 anti-human CK 19 (clone: RCK108, GA61561-2, Dako,  
864 Carpinteria, CA, USA), mouse EpCAM (14-9326-82, Thermo), and rabbit IgG antihuman  
865 vimentin (VIM): Alexa Fluor 488 (clone: D21H3, 9854BC, Cell Signaling Technology).  
866 Slides were then washed with PBS and incubated at room temperature for two hours  
867 with Alexa Fluor® 555 goat anti-mouse IgG1 antibody (A21127, Invitrogen, Carlsbad,  
868 CA, USA), and counter-stained with 4',6-diamidino-2-phenylindole (DAPI; D1306,  
869 Thermo Fisher Scientific, Waltham, MA, USA).

870

#### 871 **High content imaging and analysis:**

872 Slides were imaged as previously reported (55). Briefly, an automated high  
873 throughput microscope equipped with a 10x optical lens was used to collect 2304  
874 images across the slide. An image analysis tool, available at  
875 [https://github.com/aminnaghdlou/if\\_utils](https://github.com/aminnaghdlou/if_utils) was used to identify PACCs. Briefly, each  
876 fluorescent channel was segmented individually using adaptive thresholding and  
877 merged into one cell mask. PACCs were identified as having a nuclear diameter two-  
878 times larger than the rare cell population (four-times the area).

879

880

881

#### 882 **Single cell picking:**

883 AN Eppendorf TransferMan NK2 micromanipulator was used to collect the cell of  
884 interest in a 100  $\mu$ M micropipette. The cell was transferred into a sterile solution of 1x  
885 PBS. Single cells were stored at -80°C.

886

#### 887 **Copy number profiling:**

888 Copy number profiling from low pass whole genome sequencing samples was  
889 conducted as previously described (56, 57). Briefly, the commercially available WGA4  
890 kit (Sigma) was used for single cell whole genome amplification. Sequencing libraries  
891 were prepared with the NEB Ultra FS II with 50 ng of starting material. Cells were  
892 sequenced at a depth of 1-2 million reads on an Illumina HiSeq 4000 (Fulgent, Inc.).  
893 Raw sequencing reads were aligned with BWA-MEM to the hg19 reference. Count data  
894 was segmented via the R package DNACopy (version 1.70.0) and median values were  
895 reported for copy number ratio data.

896

#### 897 **Western Blot:**

898 PC3 parental cells or PC3 PACCs were lysed with an appropriate amount of  
899 RIPA Lysis and Extraction Buffer (Thermo Scientific) with Halt Protease and  
900 Phosphatase Inhibitor Cocktail (Thermo Scientific) for 30 minutes, rotating in 4 degrees  
901 Celsius. Lysates were spun at 21,000 xg for 15 minutes in 4 degrees Celsius and the  
902 proteinaceous supernatant was stored at -80 degrees Celsius. 50 ng of protein  
903 (measured by Pierce BCA Protein Assay, following manufacturer's protocol) (Thermo  
904 Scientific) was added to a 1:4 mixture of Laemmli Sample Buffer (BioRad) and 2-  
905 Mercaptoethanol (BioRad) and ran through a 4-20% Mini-ProTEAN TGX gel (BioRad).  
906 The gel was transferred via Trans-Blot SD Semi-Dry Transfer Cell (BioRad) onto a 0.2-  
907 micron Nitrocellulose Trans-Blot Turbo Transfer Pack using the 7-minute, 2.5A, 25V  
908 protocol designed for Mixed Molecular Weights. The blot was blocked in Casein  
909 Blocking Buffer (Sigma-Aldrich) for 1 hour at room temperature with shaking, and then  
910 transferred to primary antibody diluted in casein and incubated overnight at 4 degrees  
911 Celsius with shaking. The blot was then washed 3 times for 5 minutes each with pH 7.4  
912 Tris-Buffered Saline (Quality Biological) with 0.1% Tween 20 (Sigma) (TBST) and  
913 incubated in secondary antibody diluted 1:20,000 in Casein for 1 hour at room  
914 temperature. The blot was then washed 3 times for 5 minutes with TBST and imaged  
915 using the Odyssey Western Blot Imager (Li-Cor). See Table 1 below for antibodies  
916 used.

917

918

919

920

921

922

923

924

925

926

927 **Table 1: Western Blot Antibodies**

928



Target (Alias)	Antibody	Concentration	Secondary
SNAI1 (Snail)	Rabbit IgG Monoclonal: C15D3 (Cell Signaling Technologies 3879)	1:1000	IRDye 800CW Goat anti Rabbit IgG (Licor)
SNAI2 (Slug)	Rabbit IgG Monoclonal: C19G7 (Cell Signaling Technologies 9585)	1:1000	IRDye 800CW Goat anti Rabbit IgG (Licor)
TWIST1 (Twist-1)	Rabbit IgG Monoclonal: E7E2G (Cell Signaling Technologies 31174)	1:500	IRDye 800CW Goat anti Rabbit IgG (Licor)
VIM (Vimentin)	Rabbit IgG Monoclonal: D21H3 (Cell Signaling Technologies 5741)	1:5000	IRDye 800CW Goat anti Rabbit IgG (Licor)
CDH2 (N-Cadherin)	Rabbit IgG Monoclonal: D4R1H (Cell Signaling Technologies 13116)	1:500	IRDye 800CW Goat anti Rabbit IgG (Licor)
CLDN1 (Claudin-1)	Rabbit IgG Monoclonal: D5H1D (Cell Signaling Technologies 13255)	1:1000	IRDye 800CW Goat anti Rabbit IgG (Licor)
CDH1 (E-Cadherin)	Rabbit IgG Monoclonal: 24E10 (Cell Signaling Technologies 3195)	1:1000	IRDye 800CW Goat anti Rabbit IgG (Licor)
EPCAM (EpCAM)	Rabbit IgG Monoclonal: E678Y (Cell Signaling Technologies 93790)	1:1000	IRDye 800CW Goat anti Rabbit IgG (Licor)
ACTB (Beta-Actin)	Mouse IgG2B Monoclonal: 8H10D10 (Cell Signaling Technologies 3700)	1:5000	IRDye 680RD Goat anti Mouse IgG (Licor)

929  
930  
931  
932  
933  
934  
935  
936  
937  
938  
939  
940  
941  
942  
943  
944  
945

#### RT-qPCR:

PC3 parental cells or PC3 PACCs were lysed using the QIAshredder Kit (Qiagen), following the manufacturer's protocol. Where indicated, PC3 parental cells or PC3 PACCs were incubated in parental-conditioned media or PACC-conditioned media for 24 hours prior to lysis. RNA was extracted from lysates using an RNeasy Mini Kit

946 (Qiagen) following the manufacturer's protocol. RNA was converted to cDNA (1 ug RNA  
 947 per reaction) using the iScript cDNA Synthesis Kit (Bio-Rad) following the  
 948 manufacturer's protocol. RT-qPCR reactions were performed using SsoFast EvaGreen  
 949 Supermix (Bio-Rad), following the manufacturer's protocols, and assorted primers  
 950 (Integrated DNA Technologies) at a concentration of 10 uM. See Table 2 below for  
 951 primers used. Data was collected using the CFX96 Real-Time PCR Detection System  
 952 (Bio-Rad) with a standard cycle protocol. Gene expression was normalized to the  
 953 housekeeping gene Beta-Actin and calculated using the delta-delta Ct method. Each  
 954 biological replicate reported is an average of three technical replicates.

955 **Table 2: RT-qPCR Primers**

Target (Alias)	Forward Primer	Reverse Primer
<i>ZEB-1</i> (Zeb-1)	5-AGCAGTGAAAGAGAAGGGAATGC-3	5-GGTCCTCTTCAGGTGCCTCAG-3
<i>SNAI1</i> (Snail)	5-ACTGCAACAAGGAATACCTCAG-3	5-GCACTGGTACTTCTTGACATCTG-3
<i>SNAI2</i> (Slug)	5-CTCTGTTGCAGTGAGGGCAAG-3	5-AATATGTGAGCCTGGGCGC-3
<i>TWIST1</i> (Twist-1)	5-GTCCGCAGTCTTACGAGGAG-3	5-GCTTGAGGGTCTGAATCTTGCT-3
<i>VIM</i> (Vimentin)	5-TGCCGTTGAAGCTGCTAACTA-3	5-CCAGAGGGAGTGAATCCAGATTA-3
<i>CDH2</i> (N-Cadherin)	5-TGTGGGAATCCGACGAATG-3	5-GTCATATGGTGGAGCTGTGGG-3
<i>CLDN1</i> (Claudin-1)	5-TCTGGCTATTTTAGTTGCCACAG-3	5-AGAGAGCCTGACCAAATTCGT-3
<i>CDH1</i> (E-Cadherin)	5-ATTTTCCCTCGACACCCGAT-3	5-TCCCAGGCGTAGACCAAGA-3
<i>EPCAM</i> (EpCAM)	5-CGCAGCTCAGGAAGAATGTG-3	5-TGAAGTACACTGGCATTGACGA-3
<i>ACTB</i> (Beta-Actin)	5-ACGTGGACATCCGCAAAGAC-3	5-CAAGAAAGGGTGTAACGCAACTA-3

958  
 959  
 960  
 961  
 962  
 963

**Conditioned-Media Generation:**

964 To generate PACC-conditioned media, PC3 PACCs were generated using our  
965 standard induction-approach as described above, in a T150 tissue-culture flask. On day  
966 10 of treatment-removal, exactly 20 mL of fresh complete media were added. Exactly 24  
967 hours later, on day 11 of treatment-removal, all 20 mL of PACC-conditioned media was  
968 collected. Media was centrifuged at 1000 xg for 5 minutes to remove any debris, and  
969 then filtered through a 0.45-micron PES filter into 1 mL aliquots (to prevent freeze-  
970 thawing) that were stored at -80 degrees Celsius.

971 To generate parental-conditioned media, 1,250,000 PC3 parental cells were  
972 seeded in a T150 tissue-culture flask. After 12 hours, exactly 20 mL of fresh complete  
973 media were added. Exactly 24 hours later, all 20 mL of parental-conditioned media was  
974 collected. Media was centrifuged at 1000 xg for 5 minutes to remove any debris, and  
975 then filtered through a 0.45-micron PES filter into 1 mL aliquots (to prevent freeze-  
976 thawing) that were stored at -80 degrees Celsius.

977  
978

### 979 **Motility Assays:**

980 Transwell assays were performed using 6.5-millimeter, 8-micron, PES  
981 membranes. PC3 parental cells were seeded on the membrane at 100,000 cells/mL in  
982 250  $\mu$ L of complete media. After 12 hours, 500  $\mu$ L of testing-condition media was placed  
983 in the top and bottom wells for 24 hours. Where indicated, recombinant IL6 was added  
984 to complete media at a concentration of 0.5 ng/mL. After 24 hours, membranes were  
985 washed in PBS and nonmigrated cells were removed from the top of the membrane with  
986 a cotton-tipped applicator. Membranes were fixed in 100% ice cold methanol for 10  
987 minutes, and then stained in 0.5% crystal violet resuspended in 20% methanol for 10  
988 minutes. Membranes were washed with deionized water to remove excess stain and  
989 tiled imaging of the entire membrane was acquired with an EVOS FL Digital Inverted  
990 Fluorescence Microscope (Thermo Fisher Scientific) using a 4X objective. Image  
991 analysis to calculate percent area coverage was performed using the Phansalkar auto-  
992 local threshold method in ImageJ. Each reported biological replicate is an average of  
993 two technical replicates.

994 Wound healing assays were performed in 24-well tissue culture plates. PC3  
995 parental cells were seeded at 100,000 cells/mL in 2.5 mL of complete media. After 12  
996 hours, a P1000 pipette tip was used to create a scratch wound. After 3 washes with  
997 PBS, the scratch wounds were imaged on an EVOS FL Digital Inverted Fluorescence  
998 Microscope using a 4X phase objective. 1mL of testing-conditioned media was added  
999 for 24 hours, after which the wounds were re-imaged. Image analysis to calculate  
1000 percent wound closure was performed using the Wound Healing Size Tool Updated  
1001 plug-in in ImageJ. Each reported biological replicate is an average of two technical  
1002 replicates.

1003 Single-cell tracking assays were performed using live-cell, time-lapse microscopy  
1004 in 24-well tissue culture plates. PC3 parental cells were seeded at 25,000 cells/mL in 2  
1005 mL of complete media. PC3 PACCs were seeded 5,000 cells/mL in 2 mL of complete  
1006 media. After 12 hours, testing-condition media was added for 24 hours. Where  
1007 indicated, Tocilizumab (Selleck Chemicals) was added to complete media at a  
1008 concentration of 2.5  $\mu$ g/mL. Where indicated, Recombinant IL6 was added to complete  
1009 media at a concentration of 0.5 ng/mL. An EVOS FL Digital Inverted Fluorescence

1010 Microscope was used to take 10X phase images every 30 minutes for the 24-hour  
1011 testing-condition incubation. An on-stage environment chamber was used to maintain  
1012 cell conditions at 37 degrees Celsius, 5% CO<sub>2</sub>, and 20% O<sub>2</sub>. Images were analyzed  
1013 using the Manual Tracking and Chemotaxis Tool plug-ins in ImageJ image analysis  
1014 software. All cells analyzed were randomly selected. Cells that underwent division,  
1015 apoptosis, or moved out of frame were excluded from analysis.

1016

### 1017 **Cytokine Array:**

1018 Cytokine analysis was performed using a 274-target chemiluminescent human  
1019 cytokine antibody array, following manufacturer's protocol. (Abcam ab198496).  
1020 Nondiluted PACC-conditioned media and Parental-conditioned media were tested,  
1021 using nonconditioned media as a background control. Membranes were imaged using  
1022 the ChemiDoc XRS+ imaging system (Biorad) and densitometry data was obtained  
1023 using Image Lab Software (Biorad) with signal-specific automatic background  
1024 thresholding enabled. Background subtraction, positive control normalization differential  
1025 secretion calculations were performed following manufacturer's protocol.

1026

### 1027 **Elisa:**

1028 Quantification of IL6 present in PACC-Conditioned media was performed using  
1029 an IL6 Elisa, following the manufacturer's protocol (BioLegend 430504), with the  
1030 following alteration: sample incubation time was lengthened from 2 hours to 3 hours.  
1031 PACC-Conditioned media was diluted 1:4 in protocol buffer Assay A prior to analysis.  
1032 Data was collected using FLUOStar Omega Plate Reader (BMG LabTech) at 405 nm.

1033

### 1034 **Statistics:**

1035 Nonparametric T-Tests (Mann-Whitney) were performed to generate reported P  
1036 values. Power calculations were performed to determine appropriate sample size for *in*  
1037 *vivo* experiments, wherein an alpha value of 0.05 and a beta value of 0.8 were used.

1038

1039 NS = nonsignificant =  $P > 0.05$ .

1040 \* =  $P < 0.05$

1041 \*\* =  $P < 0.01$

1042 \*\*\* =  $P < 0.001$

1043 \*\*\*\* =  $P < 0.0001$

1044

1045

1046

1047

1048

1049

1050

1051

1052

### 1053 **References:**

1054

- 1055 1. Fidler IJ. The pathogenesis of cancer metastasis: the 'seed and soil' hypothesis  
1056 revisited. *Nat Rev Cancer*. 2003;3(6):453-8.
- 1057 2. Devasia TP, Mariotto AB, Nyame YA, Etzioni R. Estimating the Number of Men  
1058 Living with Metastatic Prostate Cancer in the United States. *Cancer Epidemiol*  
1059 *Biomarkers Prev*. 2023;32(5):659-65.
- 1060 3. Pienta KJ, Hammarlund EU, Brown JS, Amend SR, Axelrod RM. Cancer  
1061 recurrence and lethality are enabled by enhanced survival and reversible cell cycle  
1062 arrest of polyan euploid cells. *Proc Natl Acad Sci U S A*. 2021;118(7).
- 1063 4. Liu J, Niu N, Li X, Zhang X, Sood AK. The life cycle of polyploid giant cancer  
1064 cells and dormancy in cancer: Opportunities for novel therapeutic interventions. *Semin*  
1065 *Cancer Biol*. 2022;81:132-44.
- 1066 5. Zhou X, Zhou M, Zheng M, Tian S, Yang X, Ning Y, et al. Polyploid giant cancer  
1067 cells and cancer progression. *Front Cell Dev Biol*. 2022;10:1017588.
- 1068 6. Chen J, Niu N, Zhang J, Qi L, Shen W, Donkena KV, et al. Polyploid Giant  
1069 Cancer Cells (PGCCs): The Evil Roots of Cancer. *Curr Cancer Drug Targets*.  
1070 2019;19(5):360-7.
- 1071 7. White-Gilbertson S, Voelkel-Johnson C. Giants and monsters: Unexpected  
1072 characters in the story of cancer recurrence. *Adv Cancer Res*. 2020;148:201-32.
- 1073 8. Amend SR, Torga G, Lin KC, Kostecka LG, de Marzo A, Austin RH, et al.  
1074 Polyploid giant cancer cells: Unrecognized actuators of tumorigenesis, metastasis, and  
1075 resistance. *Prostate*. 2019;79(13):1489-97.
- 1076 9. Tagal V, Roth MG. Loss of Aurora Kinase Signaling Allows Lung Cancer Cells to  
1077 Adopt Endoreplication and Form Polyploid Giant Cancer Cells That Resist Antimitotic  
1078 Drugs. *Cancer Res*. 2021;81(2):400-13.
- 1079 10. Niu N, Zhang J, Zhang N, Mercado-Uribe I, Tao F, Han Z, et al. Linking genomic  
1080 reorganization to tumor initiation via the giant cell cycle. *Oncogenesis*. 2016;5(12):e281.
- 1081 11. Kim CJ, Gonye AL, Truskowski K, Lee CF, Cho YK, Austin RH, et al. Nuclear  
1082 morphology predicts cell survival to cisplatin chemotherapy. *Neoplasia*.  
1083 2023;42:100906.
- 1084 12. Shu Z, Row S, Deng WM. Endoreplication: The Good, the Bad, and the Ugly.  
1085 *Trends Cell Biol*. 2018;28(6):465-74.
- 1086 13. Niu N, Mercado-Uribe I, Liu J. Dedifferentiation into blastomere-like cancer stem  
1087 cells via formation of polyploid giant cancer cells. *Oncogene*. 2017;36(34):4887-900.
- 1088 14. Fei F, Zhang D, Yang Z, Wang S, Wang X, Wu Z, et al. The number of polyploid  
1089 giant cancer cells and epithelial-mesenchymal transition-related proteins are associated  
1090 with invasion and metastasis in human breast cancer. *J Exp Clin Cancer Res*.  
1091 2015;34:158.
- 1092 15. Liu K, Zheng M, Zhao Q, Zhang K, Li Z, Fu F, et al. Different p53 genotypes  
1093 regulating different phosphorylation sites and subcellular location of CDC25C  
1094 associated with the formation of polyploid giant cancer cells. *J Exp Clin Cancer Res*.  
1095 2020;39(1):83.
- 1096 16. Mi R, Pan C, Zhou Y, Liu Y, Jin G, Liu F. Identification of the metastasis potential  
1097 and its associated genes in melanoma multinucleated giant cells using the PHA-  
1098 ECM830 fusion method. *Oncol Rep*. 2016;35(1):211-8.

- 1099 17. Samaratunga H, Delahunt B, Egevad L, Adamson M, Hussey D, Malone G, et al.  
1100 Pleomorphic giant cell carcinoma of the urinary bladder: an extreme form of tumour de-  
1101 differentiation. *Histopathology*. 2016;68(4):533-40.
- 1102 18. Zhang D, Yang X, Yang Z, Fei F, Li S, Qu J, et al. Daughter Cells and Erythroid  
1103 Cells Budding from PGCCs and Their Clinicopathological Significances in Colorectal  
1104 Cancer. *J Cancer*. 2017;8(3):469-78.
- 1105 19. Xuan B, Ghosh D, Cheney EM, Clifton EM, Dawson MR. Dysregulation in Actin  
1106 Cytoskeletal Organization Drives Increased Stiffness and Migratory Persistence in  
1107 Polyploid Giant Cancer Cells. *Sci Rep*. 2018;8(1):11935.
- 1108 20. Xuan B, Ghosh D, Jiang J, Shao R, Dawson MR. Vimentin filaments drive  
1109 migratory persistence in polyploid cancer cells. *Proc Natl Acad Sci U S A*.  
1110 2020;117(43):26756-65.
- 1111 21. Mallin MM, Kim N, Choudhury MI, Lee SJ, An SS, Sun SX, et al. Cells in the  
1112 polyaneuploid cancer cell (PACC) state have increased metastatic potential. *Clin Exp*  
1113 *Metastasis*. 2023;40(4):321-38.
- 1114 22. Zhang L, Wu C, Hoffman RM. Prostate Cancer Heterogeneous High-Metastatic  
1115 Multi-Organ-Colonizing Chemo-Resistant Variants Selected by Serial Metastatic  
1116 Passage in Nude Mice Are Highly Enriched for Multinucleate Giant Cells. *PLoS One*.  
1117 2015;10(11):e0140721.
- 1118 23. Lv H, Shi Y, Zhang L, Zhang D, Liu G, Yang Z, et al. Polyploid giant cancer cells  
1119 with budding and the expression of cyclin E, S-phase kinase-associated protein 2,  
1120 stathmin associated with the grading and metastasis in serous ovarian tumor. *BMC*  
1121 *Cancer*. 2014;14:576.
- 1122 24. Bile-Silva A, Lopez-Beltran A, Rasteiro H, Vau N, Blanca A, Gomez E, et al.  
1123 Pleomorphic giant cell carcinoma of the prostate: clinicopathologic analysis and  
1124 oncological outcomes. *Virchows Arch*. 2023;482(3):493-505.
- 1125 25. Alharbi AM, De Marzo AM, Hicks JL, Lotan TL, Epstein JI. Prostatic  
1126 Adenocarcinoma With Focal Pleomorphic Giant Cell Features: A Series of 30 Cases.  
1127 *Am J Surg Pathol*. 2018;42(10):1286-96.
- 1128 26. Mannan R, Wang X, Bawa PS, Spratt DE, Wilson A, Jentzen J, et al. Polyploid  
1129 giant cancer cells in metastatic castration-resistant prostate cancer: observations from  
1130 the Michigan Legacy Tissue Program. *Med Oncol*. 2020;37(3):16.
- 1131 27. Trabzonlu L, Pienta KJ, Trock BJ, De Marzo AM, Amend SR. Presence of cells in  
1132 the polyaneuploid cancer cell (PACC) state predicts the risk of recurrence in prostate  
1133 cancer. *Prostate*. 2023;83(3):277-85.
- 1134 28. Mallin MM, Rolle LTA, Pienta KJ, Amend SR. Multiparameter flow cytometric  
1135 detection and analysis of rare cells in in vivo models of cancer metastasis. *Biol Methods*  
1136 *Protoc*. 2024;9(1):bpae026.
- 1137 29. Zhao Q, Zhang K, Li Z, Zhang H, Fu F, Fu J, et al. High Migration and Invasion  
1138 Ability of PGCCs and Their Daughter Cells Associated With the Nuclear Localization of  
1139 S100A10 Modified by SUMOylation. *Front Cell Dev Biol*. 2021;9:696871.
- 1140 30. Zhang S, Mercado-Urbe I, Xing Z, Sun B, Kuang J, Liu J. Generation of cancer  
1141 stem-like cells through the formation of polyploid giant cancer cells. *Oncogene*.  
1142 2014;33(1):116-28.

- 1143 31. White-Gilbertson S, Lu P, Esobi I, Echesabal-Chen J, Mulholland PJ, Goos M, et  
1144 al. Polyploid giant cancer cells are dependent on cholesterol for progeny formation  
1145 through amitotic division. *Sci Rep.* 2022;12(1):8971.
- 1146 32. Zhang D, Wang Y, Zhang S. Asymmetric cell division in polyploid giant cancer  
1147 cells and low eukaryotic cells. *Biomed Res Int.* 2014;2014:432652.
- 1148 33. White-Gilbertson S, Lu P, Saatci O, Sahin O, Delaney JR, Ogretmen B, et al.  
1149 Transcriptome analysis of polyploid giant cancer cells and their progeny reveals a  
1150 functional role for p21 in polyploidization and depolyploidization. *J Biol Chem.*  
1151 2024;300(4):107136.
- 1152 34. Bowers RR, Andrade MF, Jones CM, White-Gilbertson S, Voelkel-Johnson C,  
1153 Delaney JR. Autophagy modulating therapeutics inhibit ovarian cancer colony  
1154 generation by polyploid giant cancer cells (PGCCs). *BMC Cancer.* 2022;22(1):410.
- 1155 35. Zhang Z, Feng X, Deng Z, Cheng J, Wang Y, Zhao M, et al. Irradiation-induced  
1156 polyploid giant cancer cells are involved in tumor cell repopulation via neosis. *Mol*  
1157 *Oncol.* 2021;15(8):2219-34.
- 1158 36. Saitoh M. Involvement of partial EMT in cancer progression. *J Biochem.*  
1159 2018;164(4):257-64.
- 1160 37. Kroger C, Afeyan A, Mraz J, Eaton EN, Reinhardt F, Khodor YL, et al. Acquisition  
1161 of a hybrid E/M state is essential for tumorigenicity of basal breast cancer cells. *Proc*  
1162 *Natl Acad Sci U S A.* 2019;116(15):7353-62.
- 1163 38. Sinha D, Saha P, Samanta A, Bishayee A. Emerging Concepts of Hybrid  
1164 Epithelial-to-Mesenchymal Transition in Cancer Progression. *Biomolecules.*  
1165 2020;10(11).
- 1166 39. Haerinck J, Berx G. Partial EMT takes the lead in cancer metastasis. *Dev Cell.*  
1167 2021;56(23):3174-6.
- 1168 40. Xuan B, Ghosh D, Dawson MR. Contributions of the distinct biophysical  
1169 phenotype of polyploidal giant cancer cells to cancer progression. *Semin Cancer Biol.*  
1170 2022;81:64-72.
- 1171 41. Truskowski K, Amend SR, Pienta KJ. Dormant cancer cells: programmed  
1172 quiescence, senescence, or both? *Cancer Metastasis Rev.* 2023;42(1):37-47.
- 1173 42. Mosieniak G, Sikora E. Polyploidy: the link between senescence and cancer.  
1174 *Curr Pharm Des.* 2010;16(6):734-40.
- 1175 43. Bharadwaj D, Mandal M. Senescence in polyploid giant cancer cells: A road that  
1176 leads to chemoresistance. *Cytokine Growth Factor Rev.* 2020;52:68-75.
- 1177 44. Saleh T, Carpenter VJ, Bloukh S, Gewirtz DA. Targeting tumor cell senescence  
1178 and polyploidy as potential therapeutic strategies. *Semin Cancer Biol.* 2022;81:37-47.
- 1179 45. Saleh T, Tyutyunyk-Massey L, Gewirtz DA. Tumor Cell Escape from Therapy-  
1180 Induced Senescence as a Model of Disease Recurrence after Dormancy. *Cancer Res.*  
1181 2019;79(6):1044-6.
- 1182 46. Demaria M, O'Leary MN, Chang J, Shao L, Liu S, Alimirah F, et al. Cellular  
1183 Senescence Promotes Adverse Effects of Chemotherapy and Cancer Relapse. *Cancer*  
1184 *Discov.* 2017;7(2):165-76.
- 1185 47. Faheem MM, Seligson ND, Ahmad SM, Rasool RU, Gandhi SG, Bhagat M, et al.  
1186 Convergence of therapy-induced senescence (TIS) and EMT in multistep  
1187 carcinogenesis: current opinions and emerging perspectives. *Cell Death Discov.*  
1188 2020;6:51.

- 1189 48. Niu N, Yao J, Bast RC, Sood AK, Liu J. IL-6 promotes drug resistance through  
1190 formation of polyploid giant cancer cells and stromal fibroblast reprogramming.  
1191 *Oncogenesis*. 2021;10(9):65.
- 1192 49. Jayatilaka H, Tyle P, Chen JJ, Kwak M, Ju J, Kim HJ, et al. Synergistic IL-6 and  
1193 IL-8 paracrine signalling pathway infers a strategy to inhibit tumour cell migration. *Nat*  
1194 *Commun*. 2017;8:15584.
- 1195 50. Pienta KJ, Hammarlund EU, Austin RH, Axelrod R, Brown JS, Amend SR.  
1196 Cancer cells employ an evolutionarily conserved polyploidization program to resist  
1197 therapy. *Semin Cancer Biol*. 2020.
- 1198 51. Saini G, Joshi S, Garlapati C, Li H, Kong J, Krishnamurthy J, et al. Polyploid  
1199 giant cancer cell characterization: New frontiers in predicting response to chemotherapy  
1200 in breast cancer. *Semin Cancer Biol*. 2022;81:220-31.
- 1201 52. Middleton JD, Stover DG, Hai T. Chemotherapy-Exacerbated Breast Cancer  
1202 Metastasis: A Paradox Explainable by Dysregulated Adaptive-Response. *Int J Mol Sci*.  
1203 2018;19(11).
- 1204 53. Karagiannis GS, Pastoriza JM, Wang Y, Harney AS, Entenberg D, Pignatelli J, et  
1205 al. Neoadjuvant chemotherapy induces breast cancer metastasis through a TMEM-  
1206 mediated mechanism. *Sci Transl Med*. 2017;9(397).
- 1207 54. Chai S, Matsumoto N, Storgard R, Peng CC, Aparicio A, Ormseth B, et al.  
1208 Platelet-Coated Circulating Tumor Cells Are a Predictive Biomarker in Patients with  
1209 Metastatic Castrate-Resistant Prostate Cancer. *Mol Cancer Res*. 2021;19(12):2036-45.
- 1210 55. Marrinucci D, Bethel K, Kolatkar A, Luttggen MS, Malchiodi M, Baehring F, et al.  
1211 Fluid biopsy in patients with metastatic prostate, pancreatic and breast cancers. *Phys*  
1212 *Biol*. 2012;9(1):016003.
- 1213 56. Baslan T, Kendall J, Ward B, Cox H, Leotta A, Rodgers L, et al. Optimizing  
1214 sparse sequencing of single cells for highly multiplex copy number profiling. *Genome*  
1215 *Res*. 2015;25(5):714-24.
- 1216 57. Schmidt MJ, Prabakar RK, Pike S, Yellapantula V, Peng CC, Kuhn P, et al.  
1217 Simultaneous Copy Number Alteration and Single-Nucleotide Variation Analysis in  
1218 Matched Aqueous Humor and Tumor Samples in Children with Retinoblastoma. *Int J*  
1219 *Mol Sci*. 2023;24(10).
- 1220